Global Ocean Sediment Composition and Burial Flux in the Deep Sea

Christopher Hayes, Kassandra Costa, Robert Anderson, Eva Calvo, Zanna Chase, Ludmila Demina, Jean-claude Dutay, Christopher German, Lars-Eric Heimbürger-Boavida, Samuel Jaccard, et al.

Global Biogeochemical Cycles

RESEARCH ARTICLE
10.1029/2020GB006769

Global Ocean Sediment Composition and Burial Flux in the Deep Sea

Christopher T. Hayes[1], Kassandra M. Costa[2], Robert F. Anderson[3], Eva Calvo[4], Zanna Chase[5], Ludmila L. Demina[6], Jean-Claude Dutay[7], Christopher R. German[2], Lars-Eric Heimbürger-Boavida[8], Samuel L. Jaccard[9], Allison Jacobel[10], Karen E. Kohfeld[11], Marina D. Kravchishina[6], Jörg Lippold[12], Figen Mekik[13], Lise Missiaen[14], Frank J. Pavia[15], Adina Paytan[16], Rut Pedrosa-Pamies[17], Mariia V. Petrova[8], Shaily Rahman[1], Laura F. Robinson[18], Matthieu Roy-Barman[7], Anna Sanchez-Vidal[19], Alan Shiller[1], Alessandro Tagliabue[20], Allyson C. Tessin[21], Marco van Hulten[22], and Jing Zhang[23,24]

[1]University of Southern Mississippi, School of Ocean Science and Engineering, Stennis Space Center, MS, USA, [2]Department of Geology and Geophysics, Woods Hole Oceanographic Institution, Woods Hole, MA, USA, [3]Lamont-Doherty Earth Observatory of Columbia University, Palisades, NY, USA, [4]Institut de Ciències del Mar, CSIC, Barcelona, Spain, [5]Institute for Marine and Antarctic Studies, University of Tasmania, Hobart, TAS, Australia, [6]Shirshov Institute of Oceanology, Russian Academy of Sciences, Moscow, Russia, [7]Laboratoire des Sciences du Climat et de l'Environnement, LSCE/IPSL, CEA-CNRS-UVSQ, Université Paris-Saclay, Gif sur Yvette, France, [8]Aix Marseille Université, CNRS/INSU, Université de Toulon, IRD, Mediterranean Institute of Oceanography (MIO), Marseille, France, [9]Institute of Geological Sciences and Oeschger Center for Climate Change Research, University of Bern, Bern, Switzerland, [10]Department of Earth, Environmental and Planetary Sciences, Institute at Brown for Environment and Society, Brown University, Providence, RI, USA, [11]School of Resource and Environmental Management and School of Environmental Science, Simon Fraser University, Burnaby, Canada, [12]Institute of Earth Sciences, Heidelberg University, Heidelberg, Germany, [13]Grand Valley State University, Allendale, MI, USA, [14]Climate Change Research Centre, University of New South Wales, Sydney, Australia, [15]Division of Geological and Planetary Sciences, California Institute of Technology, Pasadena, CA, USA, [16]University of California Santa Cruz, Santa Cruz, CA, USA, [17]The Ecosystems Center, Marine Biological Laboratory, Woods Hole, MA, USA, [18]School of Earth Sciences, University of Bristol, Bristol, UK, [19]Department of Earth and Ocean Dynamics, University of Barcelona, Barcelona, Spain, [20]School of Environmental Sciences, University of Liverpool, Liverpool, UK, [21]Department of Geology, Kent State University, Kent, OH, USA, [22]Geophysical Institute, University of Bergen and Bjerknes Centre for Climate Research, Bergen, Norway, [23]School of Oceanography, Shanghai Jiao Tong University, Shanghai, China, [24]State Key Laboratory of Estuarine and Coastal Research, East China Normal University, Shanghai, China

Key Points:

- Global marine sediment composition ($CaCO_3$, opal, TOC, Fe, Hg, Ba) is presented
- Th-normalized fluxes of major and minor components in the deep sea are constrained
- Deep sea budgets and paleo-proxy applications can be refined with this compilation

Supporting Information:

Supporting Information may be found in the online version of this article.

Correspondence to:

C. T. Hayes,
christopher.t.hayes@usm.edu

Citation:

Hayes, C. T., Costa, K. M., Anderson, R. F., Calvo, E., Chase, Z., Demina, L. L., et al. (2021). Global ocean sediment composition and burial flux in the deep sea. *Global Biogeochemical Cycles*, *35*, e2020GB006769. https://doi.org/10.1029/2020GB006769

Received 28 JUL 2020
Accepted 18 MAR 2021

Abstract Quantitative knowledge about the burial of sedimentary components at the seafloor has wide-ranging implications in ocean science, from global climate to continental weathering. The use of ^{230}Th-normalized fluxes reduces uncertainties that many prior studies faced by accounting for the effects of sediment redistribution by bottom currents and minimizing the impact of age model uncertainty. Here we employ a recently compiled global data set of ^{230}Th-normalized fluxes with an updated database of seafloor surface sediment composition to derive atlases of the deep-sea burial flux of calcium carbonate, biogenic opal, total organic carbon (TOC), nonbiogenic material, iron, mercury, and excess barium (Ba_{xs}). The spatial patterns of major component burial are mainly consistent with prior work, but the new quantitative estimates allow evaluations of deep-sea budgets. Our integrated deep-sea burial fluxes are 136 Tg C/yr $CaCO_3$, 153 Tg Si/yr opal, 20Tg C/yr TOC, 220 Mg Hg/yr, and 2.6 Tg Ba_{xs}/yr. This opal flux is roughly a factor of 2 increase over previous estimates, with important implications for the global Si cycle. Sedimentary Fe fluxes reflect a mixture of sources including lithogenic material, hydrothermal inputs and authigenic phases. The fluxes of some commonly used paleo-productivity proxies (TOC, biogenic opal, and Ba_{xs}) are not well-correlated geographically with satellite-based productivity estimates. Our new compilation of sedimentary fluxes provides detailed regional and global information, which will help refine the understanding of sediment preservation.

1. Introduction

Seafloor sediments contain information about many large-scale processes in the ocean such as surface biological productivity, particle export and degradation, hydrothermal activity, and material transport from

continental weathering. These processes are often complexly intertwined and thus difficult to separate in the marine geological record. Therefore, one of the critical steps is determining the burial rate of individual sedimentary components. In particular, quantitative flux information can establish removal rates of elements from the water column and distinguish between variable transfer rates into the sediment and dilution by other phases. Reference maps of sedimentary fluxes in the global ocean have utility in expedition planning, interpretation of data sets that do not contain flux information, and investigation of global biogeochemical budgets in the modern and ancient ocean.

The flux of sediment at the seafloor can be estimated stratigraphically, using dated depth intervals and sediment density, or by normalizing sediment concentrations to the concentration of a tracer with a known vertical flux to the seafloor, such as ^{230}Th or ^{3}He. The normalization methods have several advantages over the stratigraphic method, including relative insensitivity to age model errors as well as accounting for the effects of post-depositional redistribution of sediments by deep-sea currents (François et al., 2004; McGee & Mukhopadhyay, 2013). Thorium-normalization for deriving sedimentary component fluxes was first developed in the 1980s (Bacon, 1984; Suman & Bacon, 1989), long after the pioneering expeditions of research vessels such as *Vema* and *Robert Conrad* in the 1960s and 1970s that mapped much of the ocean floor.

In the last few decades, sufficient ^{230}Th-normalized (abbreviated as Th-normalized) flux measurements have become available for incorporation into global sedimentary budgets of the main components of marine sediments, namely calcium carbonate ($CaCO_3$), biogenic opal, total organic carbon (TOC), and nonbiogenic material. For instance, in regions with high levels of sediment redistribution such as the deep Southern Ocean, biogenic opal burial rates had to be revised downwards from prior stratigraphic estimates by at least 35% after incorporating Th-normalized flux estimates (Chase et al., 2015; DeMaster, 2002), leading to a re-evaluation of the impact of climate on ocean productivity and circulation. Recent progress has been made on global marine carbon ($CaCO_3$ and TOC) budgets over glacial-interglacial timescales using Th-normalized data when possible (Cartapanis et al., 2016, 2018). Nonbiogenic material, including lithogenic material, mainly focusing on mineral aerosol dust, has also been recently tracked globally based on thorium data (Kienast et al., 2016). A global marine atlas of all the major sedimentary components using a consistent Th-normalized data set, however, has yet to be created. Additionally, the importance of metals in the ocean, either as micronutrients, proxies of past ocean properties, or contaminants, is being increasingly recognized (Anderson, 2020), and understanding their burial rates is key to appraising their biogeochemical cycling. Quantified burials rates of all sedimentary components also help constrain Earth system models (Bonan & Doney, 2018), which are essential to projections of future ocean change.

In this study, we compile an updated database of global major and trace sediment composition data from more than 12,000 globally distributed marine sediment cores. We then combine this composition information with a recently published database of Th-normalized fluxes for the Holocene (0–10 ka), containing 1,068 flux estimates across the deep ocean (Figure 1a) (Costa et al., 2020). Combining the composition and Th-normalized flux data allows us to produce new atlases of the deep-sea burial of $CaCO_3$, biogenic opal, TOC, lithogenic material, and other constituents including iron (Fe), mercury (Hg), and barium (Ba). These three trace elements were respectively chosen as examples of a micronutrient, an anthropogenic contaminant, and an element used as a paleo-proxy. This approach exemplifies how any sedimentary component of interest can be converted from relative concentrations to absolute burial fluxes. Furthermore, while this study focuses on constraining the modern ocean, a similar approach could be taken for the last glacial maximum, whose Th-normalized fluxes were also compiled by Costa et al. (2020), or for any other time-slices of interest for which Th data are available.

2. Methods

2.1. Compilations of Sediment Composition

Various global compilations of marine sediment composition have been made, and maps reflecting calculated seafloor fluxes have also been derived from these existing data sets (Berger, 1974; Broecker & Peng, 1982; Jahnke, 1996; Lisitzin, 1996). We made use here of some of the more recent prior compilations of $CaCO_3$ (Cartapanis et al., 2018; Catubig et al., 1998; Seiter et al., 2004), biogenic opal (Chase et al., 2015; Seiter et al., 2004), and TOC (Cartapanis et al., 2016; Seiter et al., 2004). We supplemented previously compiled

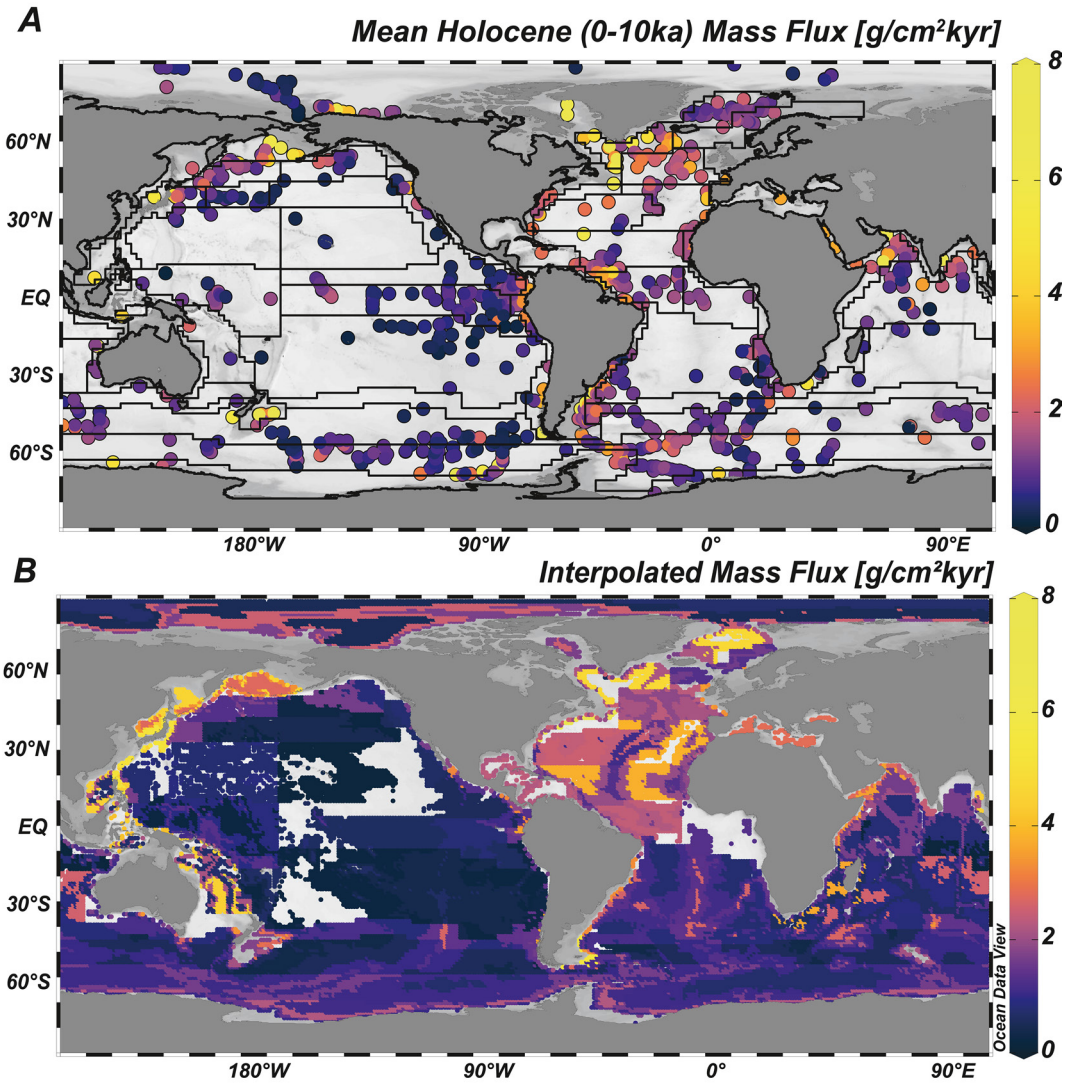

Figure 1. (a) Compiled ^{230}Th-normalized fluxes from sediment samples of Holocene age (Costa et al., 2020) overlain with the 54 biogeochemical provinces defined by Longhurst (2006) (b) Spatially interpolated ^{230}Th-normalized fluxes derived by taking the average of available measured fluxes within 145 zones defined by the biogeochemical provinces and water depth. Uncolored (white/gray) zones are shallower than 1 km or zones that do not contain any Th-normalized flux observations.

data with more recent studies or studies from ocean regions where data gaps existed, including marginal seas such as the Mediterranean, the Gulf of Mexico, the South China Sea, the Arctic Shelf seas, and others. This compilation thus provides a useful global and regional resource. The database references more than 800 publications, dissertations, cruise reports and other data reports and thus reference details for these studies are given only in the reference data archive. In the archived data, each compositional data point has a link to its source manuscript and/or its original online data archive if one exists.

The compositional database was examined using a series of quality screenings. In some cases, geographic coordinates indicated that samples were on land or near zero water depth in coastal sites; these data points were removed. In other cases, reported coordinates were curtailed or rounded to the nearest degree, causing some location uncertainty. In these cases, or where geographic coordinates were given without water depth, the correct position information was located in the Index to Marine and Lacustrine Geological Samples (IMLGS; https://www.ngdc.noaa.gov/geosamples/index.jsp). If the sample did not appear in IMLGS, water depth was estimated using the cited coordinates and ETOPO1 (http://doi.org/10.7289/V5C8276M) which

is a global bathymetry database available at 1 arc-minute resolution. Another common issue in prior data compilations was the same core being reported multiple times with different naming conventions. These were reconciled and core naming conventions used in IMLGS were used whenever possible. Samples from the Deep Sea Drilling Project, the Ocean Drilling Program and the International Ocean Discovery Program were named using the convention Leg # - Site #. One or more of the above named issues were encountered in roughly 10% of the data we compiled.

We did not exhaustively investigate the methods used to obtain compositional data, but they can be found through the links to the cited original manuscripts. The database produced by Seiter et al. (2004) gives some information on methods used for TOC analysis where available. Traditional methods to analyze total carbon in the sediments (Bisutti et al., 2004) have involved CHN elemental analyzers; TOC is then found by difference, after the sample has been acidified to remove inorganic carbon. $CaCO_3$ is often measured directly by acidifying a sample and analyzing the evolved CO_2 by coulometric titration (Mörth & Backman, 2011).

Biogenic opal (used here interchangeably with the term opal or biogenic silica), in some cases, was reported in terms of biogenic silicon (Si) or silica (SiO_2). In this study, we use the term biogenic opal to refer to biogenic, amorphous hydrated silica, freshly produced by diatoms and other siliceous plankton in the ocean (Mortlock & Froelich, 1989). When reported as biogenic silica or silicon, to convert to weight fraction of biogenic opal, we assumed a formula of $SiO_2{\cdot}0.4H_2O$ or 67 g/mol (Mortlock & Froelich, 1989). Methods to determine biogenic opal have involved leaching the biogenic opal with alkaline solutions and spectrophotometric determination of the leached Si, analysis by x-ray diffraction (XRD), Fourier Transform Infrared analysis, smear slide analysis or a normative technique in which measured Al is used to correct measured Si for a lithogenic component. The traditional alkaline leach methods were designed for high opal, siliceous oozes but may underestimate the total reactive silicon (including authigenic clays) in low opal sediments. This bias potentially leads to underestimation of total silicon burial, especially in the continental margins with low opal contents but very high accumulation rates (Rahman et al., 2017). In an intercalibration exercise, the XRD method gave biogenic silica concentrations that were on average 24% higher than the wet chemical methods (Conley, 1998). For the benefit of data users, the database contains a note as to the method used for biogenic opal when this information was available.

No general statements can be made about the methods used for trace element analysis in the compilation, as these have evolved significantly over recent decades and many methods currently exist (e.g., Sandroni et al., 2003; Wien et al., 2005; Yuan et al., 2004). For Fe, reported data included in the database are bulk elemental concentrations. For Hg, we report total Hg concentrations as they were determined in the original studies, in addition to some unpublished work from the Aix Marseille Université group. In cases where inorganic and methylated Hg were reported, we used the sum of these species. We ignored Hg concentrations above 500 ng/g, which are likely due to local Hg contamination.

With regard to barium, we focused on a fraction of the total sedimentary barium referred to as excess Ba, biogenic Ba, or Ba_{xs}. The upper continental crust contains on average 628 ppm Ba (Rudnick & Gao, 2014). Excess barium refers to the fraction that occurs in the sediments in excess of the lithogenic component. It occurs in marine sediments predominantly in the form of barite ($BaSO_4$) and is thought to form in the microenvironments of decaying organic matter in the water column (Bishop, 1988; Dehairs et al., 1980; Griffith & Paytan, 2012; Martinez-Ruiz et al., 2019) but can also be associated with iron and manganese oxyhydroxides (Arrhenius & Bonatti, 1965; Sternberg et al., 2005). The factors influencing barite preservation in sediments have yet to be clearly defined, but they may involve sediment mass accumulation rate, saturation state of bottom waters with respect to barite, and/or the redox state of the sediments (McManus et al., 1998; Monnin & Cividini, 2006; Paytan & Kastner, 1996; Van Beek et al., 2003). Despite these uncertainties, Ba_{xs} has been used as a proxy for export productivity because of its connection with the export of organic carbon to depth in the water column (Dymond & Collier, 1996; Dymond et al., 1992; François et al., 1995). To estimate Ba_{xs}, total barium in the sediments is measured and a correction for lithogenic barium is applied based on measurement of another element assumed to be found only in the lithogenic phase, such as aluminum or titanium, and an assumed lithogenic ratio of barium to the other element. Most commonly, upper continental crustal averages are used, but these ratios can vary significantly depending on the local sources of lithogenic material and therefore this correction introduces uncertainty in the final Ba_{xs} estimation. For

instance, the weight ratio of Ba/Al in lithogenic material from the Chilean margin varied from 0.003 to 0.02 (Klump et al., 2000; Reitz et al., 2004).

In this data compilation, when possible, we reported the Ba_{xs} concentrations as they were determined in the original studies. In cases where only the total Ba and Al were reported, we used the range in lithogenic Ba/Al weight ratios used in one global analysis (Eagle et al., 2003) from 0.0045 to 0.0075. The average of that range (0.006 g/g) was used first and if more than 10% of the values from a specific study resulted in a negative Ba_{xs} (i.e., the correction overcorrected for lithogenic barium), we used the lower end of the range, 0.0045. If the Ba_{xs} estimate was still negative, we did not report a Ba_{xs} value from that core. In cases where another lithogenic element was reported (Ti, Zr, etc.) instead of Al, the Rudnick and Gao (2014) upper continental crustal average ratios were used. Some authors report barite weight percent directly, which removes some of the assumptions related to corrections for the lithogenic component. These values may slightly underestimate Ba_{xs} because they do not include Ba associated with other nonlithogenic phases (e.g., organic matter or iron oxides) and because some barite is lost in the sequential leaching extraction process (Eagle et al., 2003). Using samples with estimates of both bulk Ba and Ba_{xs}, we found that the percentage correction on bulk Ba varies from 0.1% to 100% (100% meaning there is no Ba_{xs}), with a median correction of 38%. In general, in the pelagic ocean, most of the Ba is Ba_{xs}, whereas in areas of high lithogenic flux or the continental margins, Ba_{xs} can be a small fraction of total Ba (Figure S1).

There are age constraints on the compositional data, placing them in the Holocene (0–11.7 ka), for about 6% of the data. The majority of the data were reported as either "core top" or "surface sediment". This means that, especially in low accumulation rate areas, the composition may reflect conditions older than the Holocene (e.g., Mekik & Anderson, 2018). For instance, in an area with a sedimentation rate of 1 mm/kyr, the upper 1 cm of sediment may itself represent 10,000 years or more if bioturbation is mixing at least a few cm of sediment. Furthermore, the most recent sediments could be lost in the coring process. We made no attempt to assess this issue in the present compilation, and we accepted the claim of most studies to have retrieved surface sediments even if no dating was reported. Thus, while our goal is to represent fluxes in the "modern" ocean, there is some unconstrained uncertainty in the timescale represented in our reconstruction of deep-sea sedimentary fluxes.

2.2. New Composition Data

An important data gap in the Arctic Ocean was recently addressed by a surface sediment survey from the 68th expedition of RV *Akademik Mstislav Keldysh* (AMK68) to the Barents Sea (northwest Russian Arctic) in July–August 2017 (Kravchishina et al., 2019). Dried sediments from 27 stations from the upper 0.5 cm of multi-cores were analyzed at the Shirshov Institute of Oceanology, Russian Academy of Sciences, by X-ray fluorescence spectrometry for elemental composition using published methods (Budko et al., 2019; Demina et al., 2019). $CaCO_3$ and biogenic opal were analyzed at the University of Southern Mississippi by UIC coulometer for $CaCO_3$ and molybdate-blue spectrophotometry after heated alkaline extraction for biogenic opal (Mortlock & Froelich, 1989).

Another important new data set (German, 2017) presented here is from a GEOTRACES transect study in the South Pacific Ocean (GP16). Surface sediments (the 0–1 cm sections of a monocorer) were collected at 14 stations between Ecuador and Tahiti on RV *Thomas G. Thompson* (TN303) in October–December 2013. Sediments were analyzed for elemental composition, $CaCO_3$, and TOC by published methods (Honjo et al., 1995; Ingamells, 1970).

2.3. Flux Compilation Used and Its Interpolation

The Th-normalized flux compilation (Costa et al., 2020) includes only samples with satisfactory age constraints (ages within 0–10 ka specified by ^{14}C or $\delta^{18}O$) and data quality (including the provision of raw data for derived parameters). The method of Th-normalization itself has uncertainties relating to areas of high gradients in particle flux, hydrothermal input or environments with persistent nepheloid layers. Nonetheless, these uncertainties are believed to result in flux estimates with uncertainties of less than approximately 30% in nearly all ocean basins at water depths greater than 1000 m (Costa et al., 2020). The Th-normalized flux (F) is derived from the ^{230}Th activity of a dated sediment sample that is unsupported by decay within

the sediments ($^{230}Th_{xs}$). After decay-correcting the $^{230}Th_{xs}$ to the time of deposition ($^{230}Th_{xs,o}$), the flux of $^{230}Th_{xs,o}$ to the seafloor is assumed equal to the depth-integrated ^{234}U decay ($\lambda_{230}{}^{23}U$) in the overlaying water column of depth (z). Therefore, the total mass flux of sediment (in units of grams of dry sediment per square centimeter per kiloyear) can be derived with Equation 1:

$$F = \frac{\lambda_{230}{}^{234}U \times z}{{}^{230}Th_{xs,o}} \quad (1)$$

The unsupported fraction of ^{230}Th in the sediments increases with water depth and at depths shallower than about 1000 m, the supported fraction can become dominant, making it difficult to precisely constrain $^{230}Th_{xs}$. Thus, in this study we will limit our derivation of Th-normalized fluxes to cores with water depth greater than 1000 m. With a total sediment flux determined using Th-normalization (F), the flux of any sedimentary component (F_i) can be estimated by multiplying the flux by the weight fraction of the component of interest (X_i). We report all component concentrations here for weight fractions, as percentages (%), parts per million (ppm, μg/g) or parts per billion (ppb, ng/g).

$$F_i = F \times X_i. \quad (2)$$

This procedure is usually done with the Th-normalized flux and the sediment component measured on the same sediment sample. However, in general, the spatial coverage in global ocean sediments is much higher for sedimentary components than the radioisotope measurements necessary to derive Th-normalized flux. In this study, therefore, we use a spatially interpolated, deep-sea map of Th-normalized flux to derive sedimentary component fluxes at each point where a sedimentary component measurement is available. This procedure maximizes our ability to estimate sedimentary component flux in the global ocean, but relies on the assumptions used to interpolate the relatively sparse map of Th-normalized fluxes.

We assumed that two primary factors determine particle flux at the seafloor in the absence of sediment redistribution effects: (1) water depth and (2) the ocean's biogeography. Water depth plays a dominant role in biogenic particle preservation. In particular, a large flux of $CaCO_3$ is lost due to dissolution below the lysocline, the depth of which varies between different ocean basins (Archer, 1996; Key et al., 2004). Additionally, the fluxes of particulate organic carbon and to some extent other components are attenuated with depth due to bacterial respiration. Biogeography, on the other hand, plays a large role in biogenic particle production. Longhurst (Longhurst, 1995, 2006; Longhurst et al., 1995) defined 54 biogeochemical provinces in the ocean based on several environmental variables including atmospheric circulation, light availability, coastlines, water column stratification and chlorophyll *a*, among others. These provinces are not static and their borders dynamically shift with season and mesoscale variability (Reygondeau et al., 2013). Nonetheless, the biogeochemical provinces provide a useful interpolation tool for relatively sparse data because of their relation to particle flux. Many oceanographic properties relating to biogenic particle flux generally follow the Longhurst provinces including major phytoplankton type (Kostadinov et al., 2010), fluxes of TOC, biogenic opal and $CaCO_3$ to the deep sea (Honjo et al., 2008), as well as $^{231}Pa/^{230}Th$ ratios, which are sensitive to particle composition (Chase et al., 2002; Hayes et al., 2014, 2015; Pavia et al., 2018).

The spatial interpolation technique for Th-normalized fluxes was guided by the following principles. We subdivided each of the 54 biogeochemical provinces (specifically, we used the shapefile made available by the Flanders Marine Institute, 2009, based on Longhurst, 2006), into six zones corresponding to their water depth: 1,000–1,999 m, 2,000–2,999 m, 3,000–3,999 m, 4,000–4,999 m, 5,000–5,999 m, and 6,000 m or deeper. Water depths shallower than 1000 m are not used in the flux interpolation. This procedure partitions the deep sea (water depths > 1000 m) into a total of 254 zones (six depth bins per province would be 324 zones but not all provinces have seafloor at all 6 depth zones). Throughout the manuscript, we use the term "zone" to refer to these partitions. Each of the 254 zones was then assigned a Th-normalized flux equal to the average of all available ^{230}Th-normalized fluxes in that zone. The choice of 6 depth bins was made as a balance between sufficiently resolving particle flux change with depth and maximizing the number of zones containing Th-normalized flux observations. This is a form of nearest neighbor interpolation. Of the 254 possible zones, 145 zones contained at least 1 Th-normalized flux observation. 40 zones had 1 observation, 18 zones had 2 observations, 37 zones had between 3 and 5 observations, 25 zones had between 6 and 10 observations and 25 zones had more than 10 observations (ranging up to ~80 observations per zone

in areas with the highest data density; Figure S2). If a zone did not contain any Th-normalized flux observations, we did not interpolate within that zone (uncolored zones in Figure 1b). In total, this interpolation procedure extends an estimate of Th-normalized flux to about 87% of the seafloor deeper than 1000 m. The interpolated Th-normalized fluxes are available in gridded form at 1° resolution (Supporting Information).

As an assessment of the interpolation, we compared the predicted fluxes at the locations where observations were available (Figure S3). Predicted versus observed fluxes had a Pearson's correlation coefficient of 0.656, a root-mean-square error (RMSE) of 1.17 g/cm^{2}kyr and an average estimator bias of −0.04 g/cm^{2}kyr. This RMSE is roughly 15% of the range observed in Th-normalized fluxes and can be used as a minimum estimate of the uncertainty in fluxes derived in this interpolation (beyond the 30% uncertainty inherent to the method of Th-normalization mentioned above). This assessment is not ideal in that the predictions are clearly influenced by the observations, in particular for zones that have only one observation. For the zones that have adequate statistics (more than 10 observations per zone), we performed a further assessment of the predicted fluxes using a bootstraps technique. For these data-dense zones, we randomly sampled 50% of the Th-normalized flux observations within a zone and calculated the relative standard deviation of the resulting averages over 100 iterations. In this exercise, the zone averages had an average relative standard deviation of 14.8%, ranging from 4.8% to 38%. Thus, we are more confident in ascribing a roughly 15% uncertainty in the spatially interpolated Th-normalized fluxes. We also explored alternative interpolation procedures using zone medians, geometric means, and harmonic means, but the arithmetic mean produced the most consistent results in all three metrics (highest r, lowest RMSE and lowest absolute bias).

One source of uncertainty we cannot control is related to a possible observation bias in the Th-normalized fluxes. Many paleoceanographic studies specifically target drift deposits of high sediment accumulation for better temporal resolution in the sedimentary records. While the normalization to ^{230}Th corrects for these effects, there is a corresponding data gap in low accumulation sites or sites where sediments have been winnowed. Furthermore, Th-normalization is employed most often in deep water environments (Costa et al., 2020) and less so in shallow water environments (e.g., Hayes et al., 2017). Thus, this flux compilation is not employed for waters shallower than 1000 m, which can be sites of very high sediment accumulation (e.g., Bianchi et al., 2018, 2016). We contend that interpolation of the observed Th-normalized fluxes within zones for the deep sea is a reasonable solution. Even in the deep sea, future determination of Th-normalized fluxes could help fill data gap regions (Figure 1a).

We derive component fluxes for the major components (F_i in Equation 2) in two ways. First, for each sediment composition data point (X_i) in the database, a biogeochemical province was assigned based on its geographic coordinates and a Th-normalized flux (F) was assigned based on its corresponding province and water depth. This method produces an estimate of the component flux at each point for which a composition data point is available and allows us to retain as much information as possible from the sediment composition databases. Second, we also derived zone averages of the compositional data and used these along with the assigned Th-normalized fluxes to derive zone-average component fluxes. This method allows us to maximize the interpolation for both Th-normalized flux and composition and is more appropriate for deriving global integrations of the fluxes, but it masks spatial variability within zones.

We assessed the uncertainty of zone averaging on major sediment component and Ba_{xs} concentrations by comparing predicted versus observed (Figure S4), as for the Th-normalized fluxes. Since the compositional data do have significant coverage in the continental margin regions in addition to the deep sea, we used eight depth bins for compositional data including the continental margins (0–249 m, 250–999 m, 1,000–1,999 m, 2,000–2,999 m, 3,000–3,999 m, 4,000–4,999 m, 5,000–5,999 m, and 6.000 m or deeper). In these cases, most zones are relatively data dense and thus the predictions are not as sensitive to any individual observation (with Ba_{xs} being the most sparse). The metrics for $CaCO_3$% were r = 0.772, RMSE = 20.2%, and bias = 9e−17%; for opal %, r = 0.685, RMSE = 12.8%, and bias = −1.5e−16%; for TOC%, r = 0.675, RMSE = 1.1%, and bias = −1.4e−16%, and for Ba_{xs}, r = 0.620, RMSE = 54%, and bias = 46%. The propagated uncertainties, using the relative RMSE's from both Th-normalized flux and sediment composition, are roughly 25% for $CaCO_3$ flux, 22% for opal flux, 27% for TOC flux, and 56% for Ba_{xs} flux. For Fe and Hg, the uncertainty of zone averaging cannot be statistically assessed due to the sparse data.

Lastly, maps presented in the main text are equirectangular projections. For more effective viewing of the Arctic Ocean, see North Polar orthographic projections of the maps in the Supporting Information (Figures S5–S12).

3. Results

In general, the interpolation of Th-normalized fluxes (Figure 1b) shows higher fluxes in the North Atlantic basin, potentially due to the highest carbonate preservation there. The lowest fluxes are in the Pacific subtropical gyres, likely due to the combination of low biogenic particle production in the oligotrophic setting, as well as reduced particle preservation. Provinces near ocean margins, as well as some of the more productive pelagic provinces such as the eastern equatorial Pacific, have elevated fluxes. High fluxes near ocean margins may be due to elevated biogenic particle production near ocean margins but also can be related to high sedimentation of terrigenous sediments. We now turn to the composition and fluxes derived for each component of interest. We include some component-specific discussion in these subsections, while more integrative discussion topics follow in Section 4.

3.1. $CaCO_3$

The database of $CaCO_3$ content on the seafloor is the most spatially complete, with 7,792 data points distributed across all ocean basins (Figure 2a). Sediments at shallower water depths and areas with higher carbonate ion concentration in subsurface water, such as the North Atlantic, can have 80%–100% carbonate content (Archer, 1996), and near zero concentrations can be found in the deep North Pacific, the Southern Ocean and parts of the Arctic Ocean. When computed as ^{230}Th-normalized fluxes (Figures 2b and 2c), the North Atlantic still stands out as the highest flux region (>2 g/cm^{2}kyr), whereas the high carbonate content regions of the Pacific have a more subdued signal due to the lower fluxes in that basin (<1 g/cm^{2}kyr). Interestingly, the Arabian Sea has $CaCO_3$ fluxes nearly as high as the North Atlantic, and there is a sharp transition from higher to lower $CaCO_3$ fluxes in the Southern Ocean near ~55°S in the Pacific and ~40°S in the Atlantic and Indian oceans. It is known that Indo-Pacific water has become more corrosive to carbonate over the course of the Holocene, on the basis of carbonate ion reconstructions and other methods (Berelson et al., 1997; Yu et al., 2010, 2014); thus, the values shown in Figure 2, which average over the entire Holocene, may overestimate modern conditions.

3.2. Biogenic Opal

Spatial coverage in the data available for seafloor content of biogenic opal (2,948 points) is the sparsest of the major component data. Coverage is highest in the Pacific sector of the Southern Ocean, the equatorial and North Pacific Ocean, the South Atlantic Ocean, and the Arabian Sea (Figure 3a). Relatively few data are available in the subtropical South Pacific, the subtropical North Atlantic, and the Arctic Oceans. The Antarctic Polar Front (~60°S in the Pacific and ~55°S in the Atlantic and Indian Ocean basins) is characterized by the highest opal content at about 80%. The Sea of Okhotsk and the Bering Sea also demonstrate opal contents as high as 80%. Other regions of elevated opal content are the subarctic Pacific, equatorial Pacific, equatorial Atlantic, and equatorial Indian Ocean basins, but maxima in opal there tend to be no higher than 40%.

This distribution reflects both production and preservation. Greater production of opal occurs in regions where diatoms thrive (e.g., in areas of high nutrient supply due to upwelling and/or deep winter mixing). Greater preservation in sediments, however, occurs in areas with high bulk sedimentation rates that minimizes exposure opal to undersaturated conditions, and, especially in coastal settings, some incorporation of Al into opal which lowers its solubility (Ragueneau et al., 2000; Sayles et al., 2001; Tréguer & De La Rocha, 2013). For the most part, the same areas of elevated opal content stand out as areas of greater Th-normalized opal flux (Figure 3b), although the equatorial Pacific fluxes are somewhat more subdued due to the relatively low total fluxes there. The equatorial Pacific region provides a good example of how conclusions based on concentration alone will bias comparisons between sites or regions. Chase et al. (2015) found that in the Southern Ocean, opal flux rates were largely determined by Southern Ocean frontal dynamics

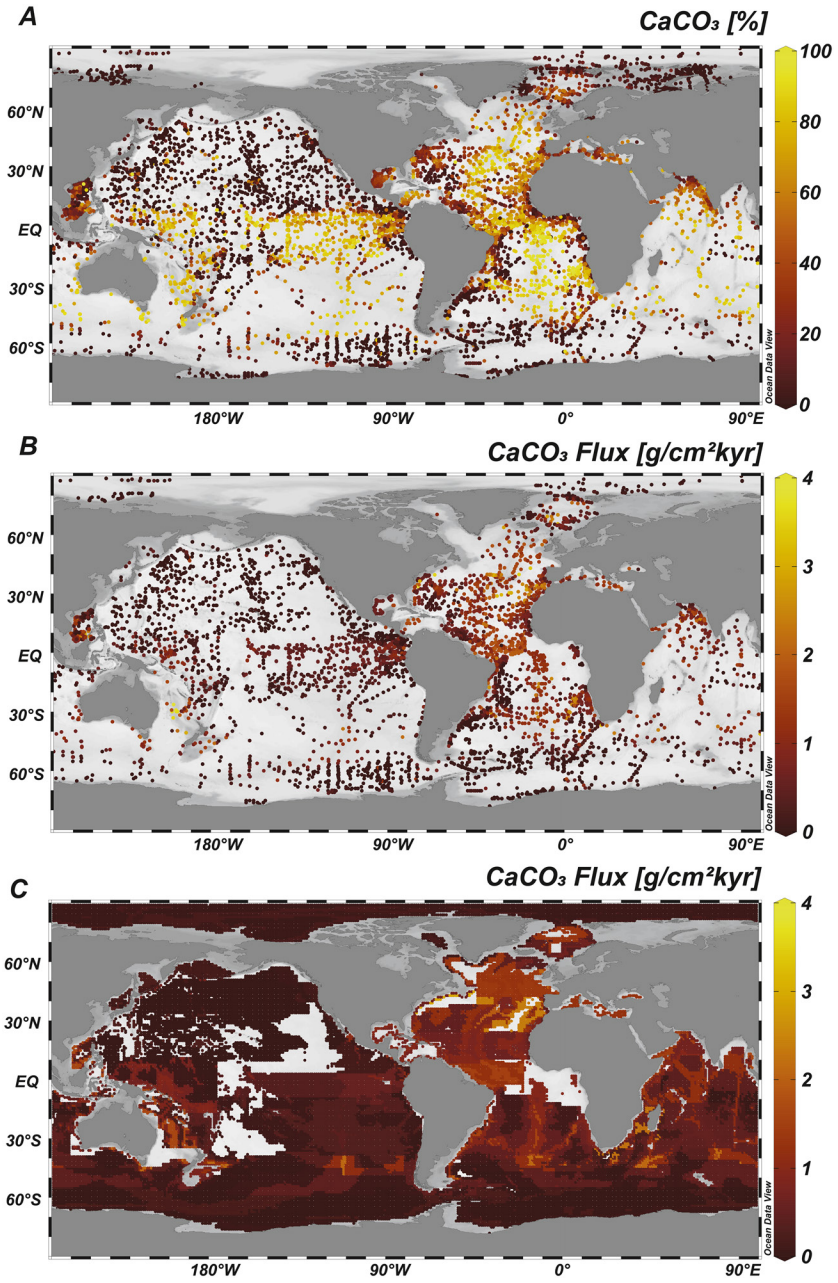

Figure 2. (a) Weight percentage of $CaCO_3$, (b) flux of $CaCO_3$ in surface sediments using spatially-interpolated Th-normalized fluxes with discrete $CaCO_3$% observations, and (c) flux of $CaCO_3$ using spatially-interpolated Th-normalized fluxes and spatially-interpolated $CaCO_3$% values. Uncolored (white/gray) zones are shallower than 1 km or zones that do not contain any Th-normalized flux observations.

including the annual number of ice-free days. This new compilation may be useful in determining the controls on biogenic opal flux in other regions.

3.3. Total Organic Carbon

The distribution of available surface sediment TOC content (Figure 4a) is similar to that of biogenic opal, with much more data for the subpolar and polar North Atlantic and a fairly high density of data on many of the continental shelves. While there are more data available for TOC (6,425 points) than opal, the high concentration of TOC data on the shelves is at the expense of deep ocean data, particularly in the South Pacific.

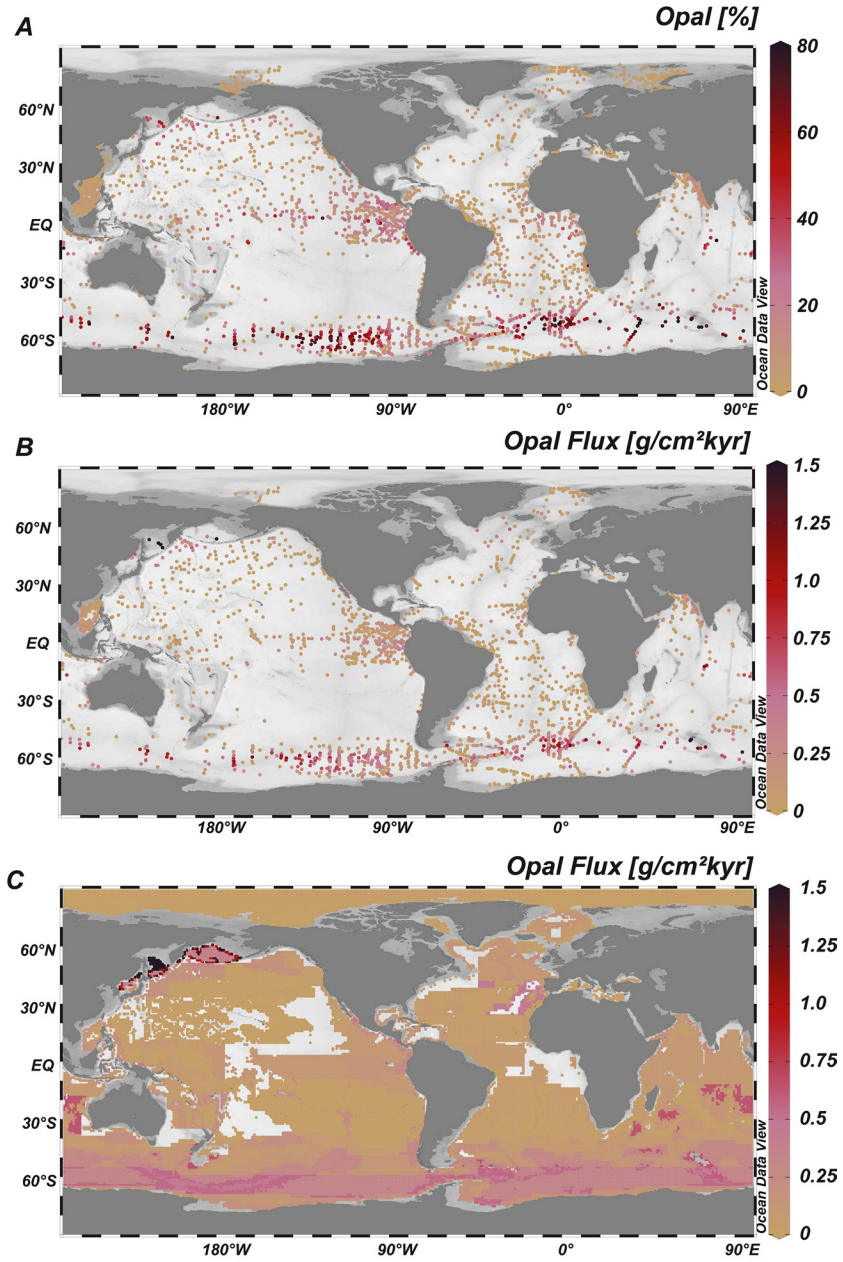

Figure 3. (a) Weight percentage of opal, (b) flux of opal in surface sediments using spatially-interpolated Th-normalized fluxes with discrete opal % observations, and (c) flux of opal using spatially-interpolated Th-normalized fluxes and spatially-interpolated opal % values. Uncolored (white/gray) zones are shallower than 1 km or zones that do not contain any Th-normalized flux observations.

The global mean TOC content is 1.1%, and the median is 0.63%, indicating the influence of relatively high (>2%) TOC contents found on the continental shelves in the average. With regard to the continental shelves, it is important to note that a significant portion of this organic matter, in particular for deltaic sediments, is terrigenous in origin, as inferred by $\delta^{13}C$ information (Burdige, 2005). Recently employed machine-learning techniques also may be useful in predicting TOC contents in unobserved areas (Lee et al., 2019; Restreppo et al., 2020).

High TOC flux areas (Figures 4b and 4c) stand out near many of the eastern margins of basins, the Bering Sea, the eastern Equatorial Pacific and the Arabian Sea. Due to the strong effects of preservation on TOC in sediments (Schoepfer et al., 2014), the flux patterns here are likely decoupled from surface ocean

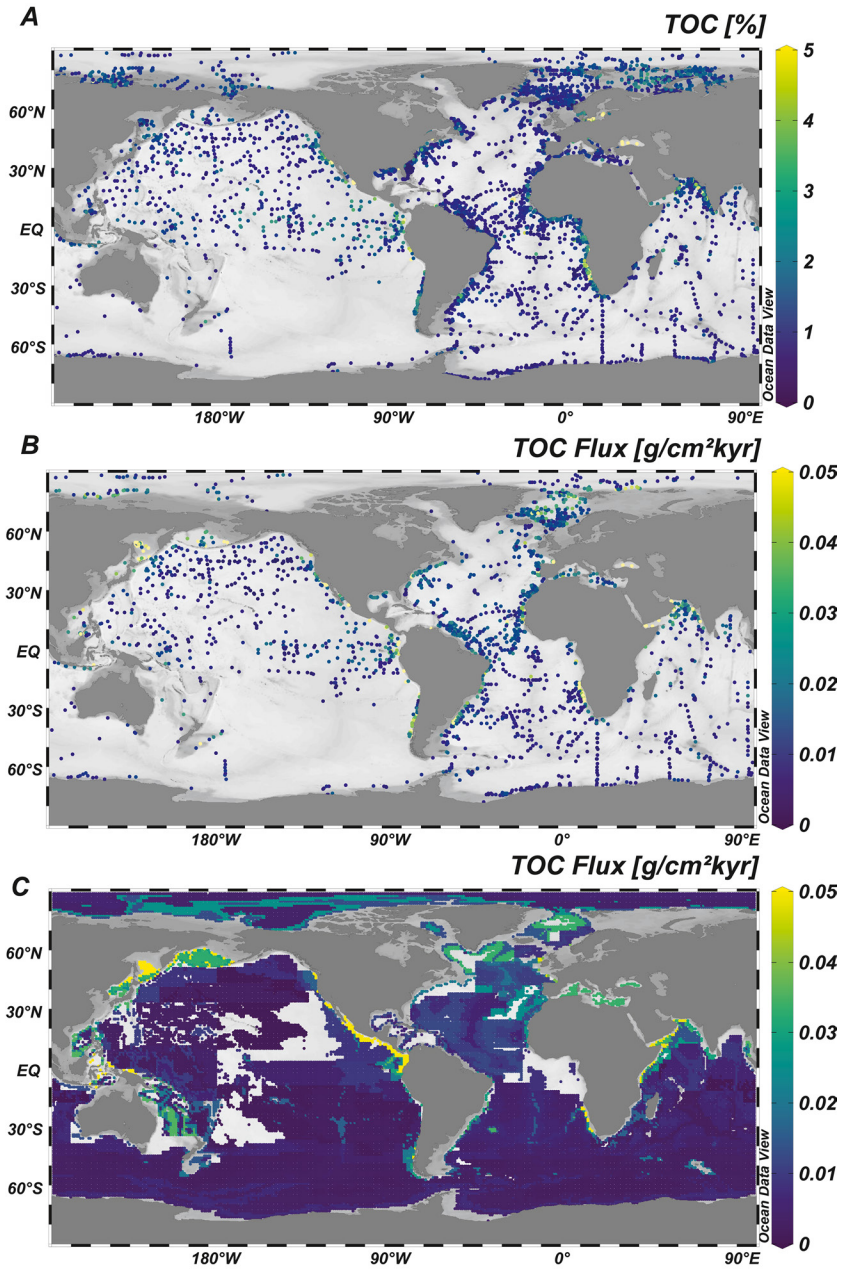

Figure 4. (a) Weight percentage of TOC, (b) flux of TOC in surface sediments extrapolated using discrete TOC % observations, and (c) flux of TOC using spatially-interpolated Th-normalized fluxes and spatially interpolated TOC observations. Uncolored (white/gray) zones are shallower than 1 km or zones that do not contain any Th-normalized flux observations. TOC, total organic carbon.

productivity patterns. However, these fluxes are useful in constraining global carbon budgets as we will pursue in the discussion.

3.4. Nonbiogenic Material and Iron

We estimated the weight percentage of nonbiogenic material (Figure 5a) by using the zone averaged percentages of $CaCO_3$, opal, and organic matter (calculated as 1.88 g organic matter/g TOC; Lam et al., 2011) and assuming nonbiogenic material was the remainder of the total weight. Nonbiogenic material here likely represents predominantly lithogenic material, such as aluminosilicates, except in areas with significant

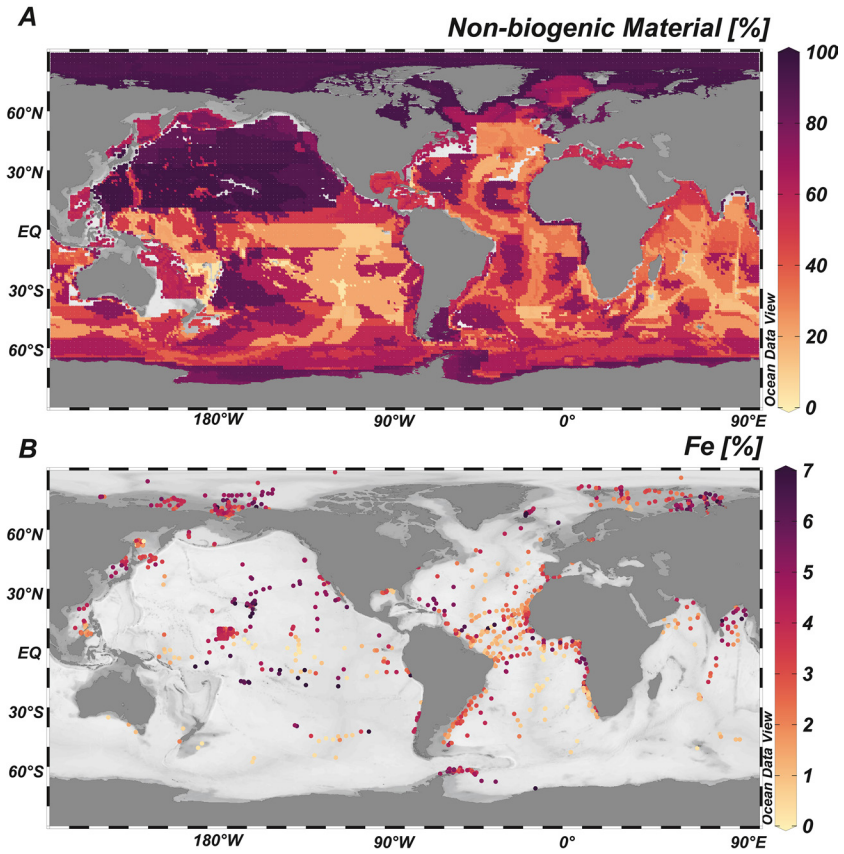

Figure 5. The weight fractions of nonbiogenic material (a) and Fe (b) in the global ocean. The Fe estimates are from discrete cores in the database and the nonbiogenic material is based on the 1° resolution interpolated major component fractions, assuming nonbiogenic material is the residual between 100% and the percentages of $CaCO_3$, opal, and organic matter.

authigenic metal accumulation, such as reducing sediments of the coastal ocean, or areas receiving hydrothermal input. Less nonbiogenic material (~10%–20%) is found on the mid-ocean ridges because of the higher percentage of $CaCO_3$ preserved there. In all the deep basins, the nonbiogenic percentage increases with depth and approaches 90%–100% in the deep North Pacific and Arctic basins, in part because of the lack of other particle phases preserved there.

We present these data together with the Fe weight percentage compilation, containing 1,210 points (Figure 5b), since Fe in the ocean is predominantly associated with lithogenic and authigenic sediments. Fe and our estimate of nonbiogenic material have similar distributions overall, with higher Fe content in all deep basins as well as in the Arctic Ocean and most marginal seas. Fe is on average 3.9% in the upper continental crust (Rudnick & Gao, 2014), but this Fe fraction will of course vary depending on the source of the lithogenic material. The average lower continental crust is 6.7% Fe (Rudnick & Gao, 2014); the average oceanic crust (mid-ocean ridge basalt) is 8.1% Fe (White & Klein, 2013); and metalliferous sediments underlying sites of hydrothermal vents can be considerably more enriched (Boström et al., 1969). The Fe concentrations of samples included in this ocean sediment database range from 0.02% to ~20% Fe, with a median of 3.1%. The distribution of the Fe/Al ratio (Figure 6; note not all Fe data points had available Al data) is one indication of the source of iron, as the upper continental crust has a Fe/Al weight ratio of 0.48 (Rudnick & Gao, 2014) and mid-ocean ridge basalts have a ratio of 1.01 (White & Klein, 2013). Excluding highly Fe enriched samples with Fe/Al > 1.5, about 50% of the ratio observations are near or below the upper continental crust average. Areas with enriched Fe/Al ratios include GEOTRACES expedition GP16 (~10°–20°S, 90°–140°W), which underlies an extended hydrothermal plume emanating westward from the East Pacific Rise (Fitzsimmons et al., 2017; Resing et al., 2015).

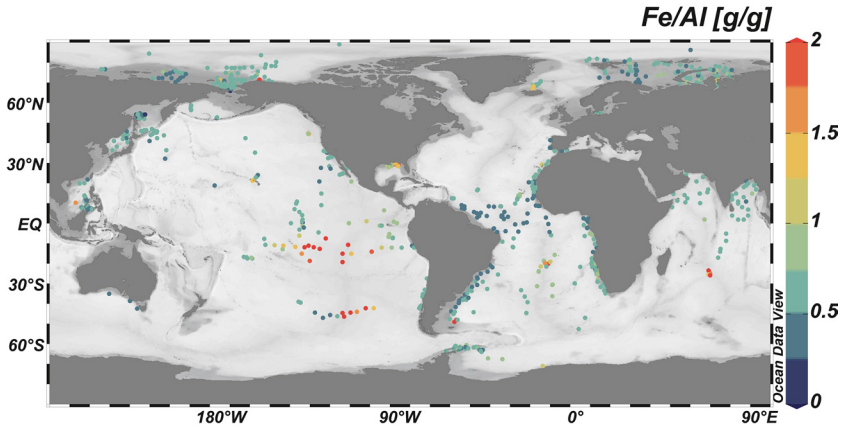

Figure 6. Fe/Al weight ratio in the global sediment composition database. The upper continental crust has an average ratio of 0.48 g/g and mid-ocean ridge basalts have a ratio of 1.01 g.g. Note in comparison to Figure 5, only a subset of Fe datapoints had available Al data.

Additional enriched areas include other sites from Southern East Pacific Rise, the Mid-Atlantic and Central Indian Ridges, sites near basaltic oceanic islands, including Hawaii and Iceland, as well as several continental margin areas including the Sea of Cortez, the northern Gulf of Mexico, and the shallow Arctic seas. This demonstrates that both hydrothermal input and coastal authigenic metal formation have imprints on the global Fe distribution in addition to lithogenic material such as dust.

When converted to flux, the overall similarity of nonbiogenic material and Fe flux is again apparent (Figure 7). Despite higher concentrations in the North Pacific basin, the nonbiogenic material and Fe fluxes are lower in the North Pacific Ocean than in the deep North Atlantic Ocean. The higher fluxes in the Atlantic basin are likely indicative of the large lithogenic flux of Saharan dust to the North Atlantic Ocean in addition to other coastal sources, such as rivers or margin sediments. Many of the marginal seas have elevated Fe and nonbiogenic material fluxes reflecting coastal sources.

3.5. Mercury

Spatial coverage for surface sediment Hg concentrations is the most sparse of the components considered here (320 observations; Figure 8a). Observations in the Northern Hemisphere and on continental margins are much more prevalent than in the Southern Hemisphere or in the central basins. In the Atlantic Ocean, high continental runoff may cause higher sediment Hg levels on its continental shelves (58 ± 97 ppb) compared to its deep basin sediments (38 ± 21 ppb). In the Pacific Ocean, there are higher Hg concentrations in the Humboldt Upwelling System (202 ± 85 ppb) compared with the deep Pacific Ocean (71 ± 46 ppb), and this may be due to higher particulate Hg export in the productive upwelling region. Smaller basins, such as the Black Sea and the Mediterranean Sea are characterized by relatively high sediment Hg concentrations (149 ± 47 ppb and 86 ± 76 ppb, respectively). As more data on Hg concentrations in seawater become available (e.g., Bowman et al., 2015, 2016; Cossa et al., 2009, 2018; Kim et al., 2017; Rosati et al., 2018), we may be able to further link some of these basin sedimentary differences to water column processes.

While the conversion to Hg flux also results in sparse estimates, both with discrete Hg observations (Figure 8b) or zone-averaged Hg observations (Figure 8c), we consider how the Hg fluxes derived here compare with other global or basin-wide estimates which remain highly uncertain. Note in Figure 8c that the South Pacific Subtropical Gyre is a single Longhurst province (Figure 1) between the margins of Australia and South America. With observations only on the western edge of this province, the interpolation scheme extends the flux estimate to much of the South Pacific. When integrated across zones, our estimate provides nearly full coverage of the Arctic Ocean deeper than 1,000 m (Figure 8c and Figure S11). The integrated Arctic Hg flux is 4.4 ± 0.7 Mg/yr, which is consistent with a recent estimate in the deep Arctic (4 ± 3 Mg/yr) that derived fluxes by assuming a constant sedimentation rate (Tesán Onrubia et al., 2020). The uncertainty in our flux estimate is a minimum as it only accounts for uncertainty in the Th-normalized flux

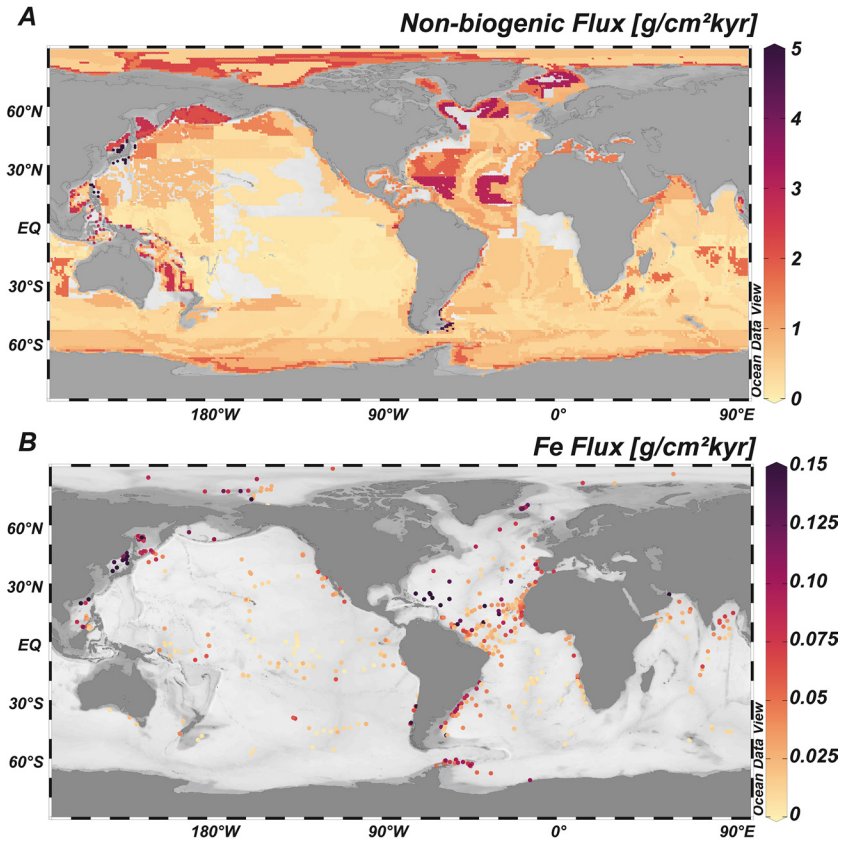

Figure 7. Th-normalized flux of (a) nonbiogenic material based on spatially interpolated mass flux and $CaCO_3$, opal and organic matter observations and (b) Fe flux based on spatially interpolated mass flux and discrete Fe observations.

interpolation. There are too few Hg data presently available to statistically assess the uncertainty in Hg interpolation. While coverage across the interpolation zones globally is not complete, we can nonetheless attempt a global integration. To do this, we assumed the average fluxes in the North Pacific apply to the entire North Pacific, the average fluxes in the South Pacific apply to the entire South Pacific and Indian Ocean, and the average fluxes in the North Atlantic apply to the entire Atlantic basin (using surface areas defined by ETOPO1). This produces a global deep-sea burial rate of 220 ± 40 Mg Hg/yr. Because the Th-normalized flux observations are confined to the deep ocean (>1000 m), our integration misses a likely considerable flux on the continental shelves and upper continental slopes. Our estimate of deep-sea Hg burial is close to another recent study, 360 Mg/yr (Zhang et al., 2015), and significantly smaller than the 600 Mg/yr (Outridge et al., 2018) and 1540 Mg/yr (Amos et al., 2014) made in other studies. It will require more observations of deep-sea and continental margin Hg concentrations to resolve this issue.

3.6. Excess Barium

Our database contains 1,457 estimates of Ba_{xs}. As a relatively minor component of the sediments (0–~5000 ppm), Ba_{xs} weight fractions are influenced by dilution of the varying total sediment flux, for instance with lower weight fractions in the North Atlantic versus the North Pacific on average (Figure 9a). When converted to flux (Figure 9b), there are higher Ba_{xs} fluxes in the eastern equatorial Pacific, the subarctic Pacific, across several frontal zones in the Southern Ocean, and in the Arabian Sea, with lower fluxes found in the central Pacific, the tropical Atlantic and the Arctic. Importantly, barite, the main carrier of Ba_{xs}, is not preserved in sulphate reducing sediments (Riedinger et al., 2006; Torres et al., 1996); hence, areas like upwelling zones or restricted basins may not preserve the original deposition flux. There may also be preservation effects on Ba_{xs} accumulation under oxic or suboxic conditions, including bottom waters undersaturated with respect to barite, which have not yet been thoroughly determined (McManus et al., 1998; Paytan & Griffith, 2007;

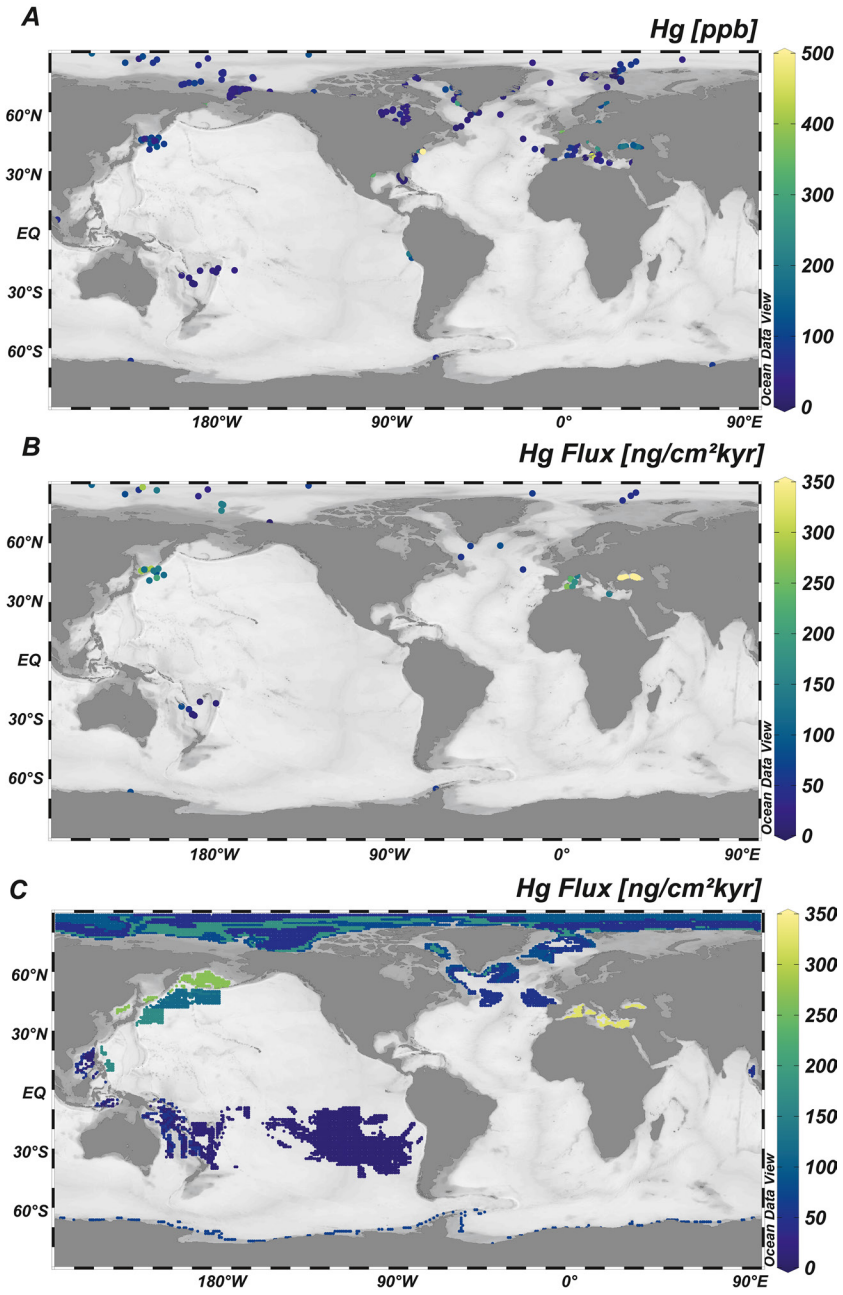

Figure 8. (a) Hg concentrations, (b) flux of Hg in surface sediments extrapolated using discrete Hg observations, and (c) flux of Hg using spatially-interpolated Th-normalized flux and zone-averaged Hg observations. Note in many cases here a limited number of observations are interpolated across relatively large interpolation zones, for example, in the South Pacific Subtropical Gyre and around Antarctica.

Serno et al., 2014; Van Beek et al., 2003). We examine the relationship between our derived Ba_{xs} fluxes and indicators of biological productivity in the discussion.

The spatial coverage of Ba_{xs} flux observations is sufficient to estimate the global deep-sea burial (Figure 9c) as 2.6 ± 1.4 Tg Ba xs/yr. This is very close, though with a significant uncertainty, to a previous estimate of 2.5 Tg/yr (Dickens et al., 2003; Paytan & Kastner, 1996). This prior estimate assumed a steady-state between Ba burial and the supply of dissolved Ba by rivers (estimated as 2.2 Tg/yr) and hydrothermal vents (estimated as 0.5 Tg/yr). Paytan and Kastner (1996) based these fluxes on data available at the time from the Congo, Amazon and Mississippi Rivers (Edmond et al., 1978) and hydrothermal vent observations from the East

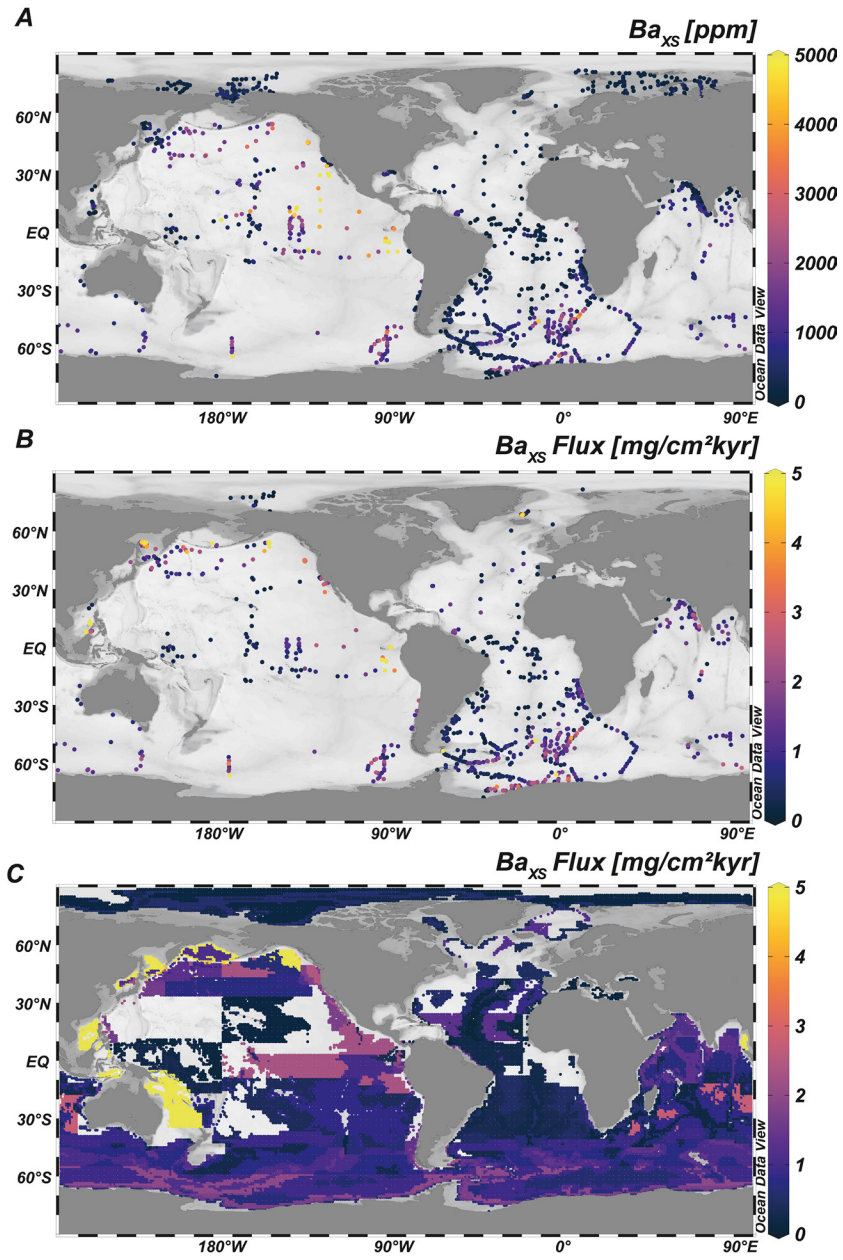

Figure 9. (a) Ba_{xs} concentration, (b) Ba_{xs} fluxes based on spatially-interpolated Th-normalized fluxes and discrete Ba_{xs} observations and (c) Ba_{xs} flux based on spatially-interpolated Th-normalized fluxes and zone-averaged Ba_{xs} observations.

Pacific Rise (Von Damm et al., 1985). The magnitude of Ba sources is currently being assessed (e.g., Horner et al., 2020), including evidence for other sources such as submarine groundwater discharge or cold seeps. Because of the uncertainty in our Ba burial estimate, it is premature to conclude whether or not there is a steady-state balance between burial and known sources.

4. Discussion

4.1. Deep-Sea Burial of $CaCO_3$, Opal, and TOC

Using the spatially interpolated flux maps of $CaCO_3$, opal and TOC, we can integrate across the global ocean and estimate a burial flux of these components to the deep sea (>1 km depth) based entirely on

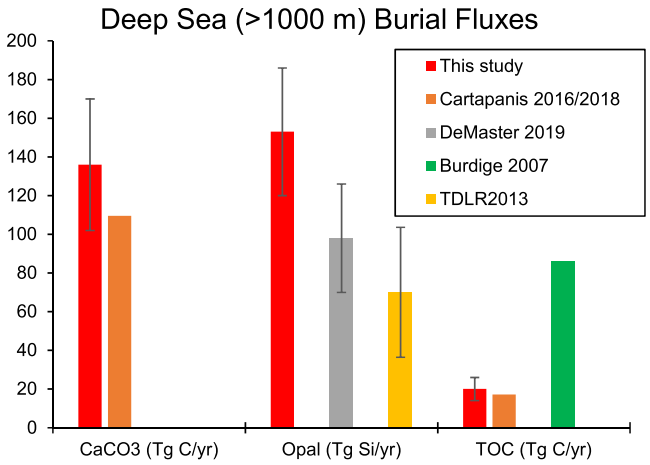

Figure 10. Comparison of globally integrated deep-sea (>1,000 m) fluxes of $CaCO_3$, opal, and TOC from this and other studies (Burdige, 2007; Cartapanis et al., 2018, 2016; DeMaster, 2019; TDLR2013 = Tréguer & De La Rocha, 2013).

Th-normalized fluxes. These fluxes of C and Si are critical to understanding their global cycling and turnover rates. Our Th-normalized flux interpolation only extends to the 87% of the seafloor for which data are available and thus our summed burial rates will underestimate global burial.

4.1.1. $CaCO_3$ Burial

The deep-sea burial of $CaCO_3$ derived from our interpolation is 136 ± 34 Tg C/yr. Cartapanis et al. (2018) discuss that the range of existing deep-sea $CaCO_3$ burial estimates is 100–150 Tg C/yr, strikingly in-line with our estimate (Figure 10). To examine our estimate further, we look at the relative contributions of the ocean basins to the total $CaCO_3$ burial. In our flux estimations, the following fractions of $CaCO_3$ flux were buried in the Atlantic (40%), Pacific (22%), Indian (20%), Southern (17%), and Arctic (0.4%) Oceans. The basin boundaries were defined using the Longhurst provinces in Figure 1. These percentages compare well to the ranges for the basin $CaCO_3$ flux percentages from Cartapanis et al. (2018), based on a smaller data set of Th-normalized fluxes, and from the model of Dunne et al. (2012): Atlantic (41%–48%), Pacific (25%–27%), Indian (24%–34%), Antarctic (0%), and Arctic (1%). The main difference in this comparison is that Cartapanis et al. (2018) calculated the Antarctic Ocean as only south of 60°S, whereas in our calculation the Longhurst provinces consider the Southern Ocean south of roughly 40°S. The continental shelves and shallow water environments are expected to have a $CaCO_3$ burial rate of around 150 Tg C/kyr for a total of ~300 TgC/yr (Milliman, 1993). Thus, our estimates of $CaCO_3$ burial appear to be consistent with previous work.

4.1.2. Biogenic Opal Burial

The deep-sea burial of opal derived here, given in terms of Si, is 153 ± 33 Tg Si/yr. Of this total, the Southern Ocean (>40°S) deep-sea Si burial is 75 ± 17 Tg Si/yr. This is consistent, within uncertainties, with that derived by Chase et al. (2015) for the deep Southern Ocean of 64 ± 28 Tg Si/yr. This is as to be expected as Chase et al. (2015) used a very similar approach as the present study, involving Th-normalized opal flux observations interpolated across biological provinces. Outside of the Southern Ocean then, our study estimates a biogenic opal burial of 78 ± 17 Tg Si/yr in the deep sea north of 40°S. Because of the finding that XRD methods for opal determination were significantly higher than other methods (Conley et al., 1998), as a sensitivty analysis we re-ran the interpolation process, excluding data points produced by the XRD method. This did not significantly alter the results within our uncertainty (the resulting fluxes excluding XRD data were total deep-sea burial of 152 ± 33 Tg Si/yr, Southern Ocean burial of 71 ± 16 Tg Si/yr and non-Southern Ocean burial of 81 ± 18 Tg Si/yr). Our estimated deep-sea burial of 153 Tg Si/yr is a significant upward revision from previous estimates of 98 Tg Si/yr (DeMaster, 2019) and 70 Tg Si/yr (Tréguer & De La Rocha, 2013). We have determined that most of the upward revision is due to increased burial rates in the non-Antarctic deep sea.

The latest prior estimates in the literature for deep-sea biogenic Si burial outside of the Southern Ocean mainly derive from the work of DeMaster (1981), who calculated a non-Antarctic deep-sea burial of 29 Tg Si/yr. This value has been used without significant modification in most subsequent assessments of the global silica cycle (DeMaster, 2002; Ragueneau et al., 2000; Tréguer & De La Rocha, 2013; Tréguer et al., 1995). DeMaster (2019) used a slightly higher non-Antarctic deep-sea burial of 34 Tg Si/yr. Still, this estimate is more than a factor of 2 lower than our estimate of 78 Tg Si/yr. DeMaster (1981) estimated this burial flux based on basin-averaged biogenic silica content and bulk mass accumulation rates for basins assumed to be responsible for the majority of deep-sea silica burial, namely the Bering Sea (14 Tg/yr), the North Pacific (8.4 Tg/yr), the Sea of Okhotsk (5.6 Tg/yr), and the Equatorial Pacific (0.6 Tg/yr). A maximum burial estimate for the rest of the deep sea, assumed to be very low in silica content, was also included (<0.2 Tg/yr). The Si burial rates from our interpolation (using only water depths >1000 m) for these basins are: Bering Sea (2.6 Tg/yr), North Pacific (4.4 Tg/yr, within the geographic box used by DeMaster, 1981, bound by the northern margin and 35°N from Asia to 170°E and the box bound by the northern margin and 42°N between 170°E and North America), Sea of Okhotsk (2.2 Tg/yr), and the equatorial Pacific (5.6 Tg/yr, using

the box bound by 3°N, 6°S, 170°W, and 79°W, representing a similar area to that considered by DeMaster, 1981). The remainder of the deep sea north of 40°S contains burial of 61 Tg Si/yr. Thus, our estimates revise downward (by factors less than 10) the estimates from the Bering Sea, the North Pacific and the Sea of Okhotsk, possibly due to the impact of sediment focusing on the mass accumulation rates assumed by DeMaster (1981) for these regions. At the same time, our estimates are significantly higher in Si burial in the Equatorial Pacific and the remaining ocean. Not available to DeMaster (1981) at the time, our new compilation of opal concentration data (2,399 deep-sea points) shows there are in fact many regions outside of the assumed "hot spots" for opal burial that contain opal in excess of 10%, such as the northeast Atlantic and equatorial Indian (Figure 3). Additionally, Th-normalized burial rates constrained for nearly all (87%) of the deep sea can properly account for the magnitude of opal burial even in sediment of low opal concentration. By basin, our calculated deep-sea opal burial was found in the following: 11% (Atlantic), 24% (Pacific), 15% (Indian), 49% (Southern), and 0.2% (Arctic).

Recent estimates of biogenic silicon burial on the continental margins range from 235 ± 118 Tg Si/yr (Rahman et al., 2017; Treguer et al., 2021) to 140 ± 30 Tg Si/yr (DeMaster, 2019). The burial of silicon associated with siliceous sponges, also mainly found on continental margins, may be another significant flux (48 Tg Si/yr according to Maldonado et al., 2019 or 25 Tg Si/yr at most, according to DeMaster, 2019). Thus, our estimate of deep-sea biogenic Si burial of 153 Tg/yr could be on par to the continental margin sink in global ocean Si burial. In other words, roughly 50% of the burial sink of Si in the ocean occurs in the deep sea.

4.1.3. TOC Burial

Our deep-sea TOC burial rate is 20 ± 6 Tg C/yr. This is similar to the estimate of Cartapanis et al. (2016) of 17 Tg C/yr that used Th-normalized fluxes where possible. In contrast, another available estimate of deep-sea (>1000 m) organic carbon burial is higher, 86 Tg C/yr (Burdige, 2007), based on organic carbon remineralization rates (Figure 10). Another study (Dunne et al., 2007) estimated TOC burial of 12 TgC/yr in waters deeper than 2000 m based on available composition data and bulk accumulation rates (Jahnke, 1996). The equivalent flux (below 2 km) in our assessment is 17 ± 5 TgC/yr, which is in line with the Dunne et al. (2007) estimate. The fractional contributions to TOC burial for the different basins in our estimate are: Atlantic (28%), Pacific (39%), Indian (15%), Southern (15%), and Arctic (3%). This is fairly similar to the fractional contribution to surface area in the deep sea using the Longhurst definitions: Atlantic (21%), Pacific (41%), Indian (13%), Southern (22%), and Arctic (4%), perhaps indicating a slightly outsized contribution from the Atlantic and reduced contribution from the Southern Ocean to the global deep-sea TOC burial on a per area basis. Many studies recognize that a large proportion of organic carbon is buried in the continental margin environment, such as Burdige's (2007) estimate of a 222 TgC/yr in water shallower than 1000 m, giving a total ocean burial rate of 309 TgC/yr (Figure 10). In summary, the deep-sea fluxes derived here will help constrain budgets of C and Si, though the significant coastal ocean fluxes likely cannot be constrained by Th-normalization and should be pursued by other methods.

4.2. Imprints of Biological Productivity in Sedimentary Fluxes

As these have all been used for paleo-proxies of biological productivity in the ocean, we compared our sedimentary fluxes of opal, TOC and Ba_{xs} to estimates of net primary productivity (NPP) and export productivity (EP) in the modern ocean (maps of the NPP and EP used shown in Figure S15). For net primary productivity, we used the satellite-based Carbon, Absorption, and Fluorescence Euphotic-resolved (CAFE) algorithm (Silsbe et al., 2016), using monthly data from the Oregon State University Ocean Productivity webpage (http://sites.science.oregonstate.edu/ocean.productivity/) averaged over 1 decade (2003–2012), which provided estimates at 1/6°-resolution. For export productivity, we used a satellite- and ocean tracer observation-constrained estimate of the flux of particulate organic carbon out of the euphotic zone (DeVries & Weber, 2017), available at 2°-resolution. Each flux data point (i.e., as plotted in Figures 3b, 4b, and 9b) in our database was matched with the closest grid point in the NPP and EP estimates. We also compared discrete observations for which Th-normalized flux (at >1000 m water depth) and component composition were measured on the same core ($n = 444$ for opal flux, $n = 247$ for TOC flux, and $n = 211$ for Ba_{xs} flux) to NPP and EP, to remove the uncertainty associated with spatial interpolation. It is only for the relationships with these directly observed component fluxes that we report correlation statistics below.

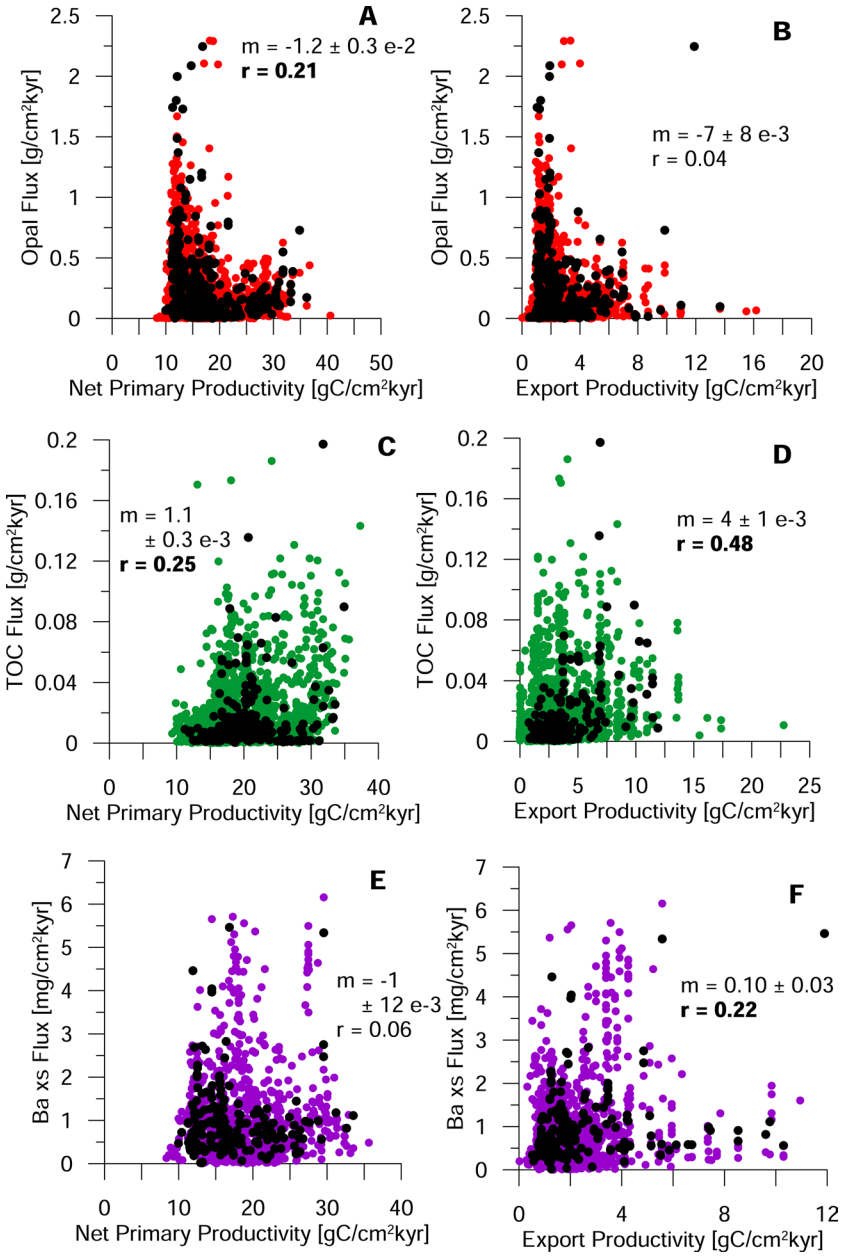

Figure 11. (a–f, respectively) Comparisons and linear correlation analyses between deep-sea opal flux, total organic carbon (TOC) flux, and Ba_{xs} flux derived from the present study with net primary productivity (a, c, e) and export productivity estimates (b, d, f) (DeVries & Weber, 2017; Silsbe et al., 2016). Colored points are based on spatially-interpolated fluxes and black points are direct component and Th-normalized flux observations for the same core. The insets display the linear regression slope (*m*, with e indicating power of 10 exponent) and Pearson correlation coefficient (*r*, bold indicating statistical significance at 95% confidence).

Despite their association with biological productivity, opal flux, TOC flux, and Ba_{xs} flux all have weak linear correlations with NPP and EP (Figure 11; all r values < 0.5). For opal, there is an apparent negative relationship (which is statistically significant at 95% confidence for opal flux vs. NPP) that can be seen with the highest opal fluxes mostly on the lower end of the spectra of NPP (10–15 g C/cm^{2}kyr) and EP (2–3 g C/cm^{2}kyr). This is largely due to areas of the Southern Ocean which are relatively low in NPP and EP on the annual average but are among the most productive regions for diatoms and opal particle flux (Honjo et al., 2008) (Figure 3). In TOC, there are weak but significant positive linear correlations between TOC flux and NPP and EP, although a large number of points with very low TOC flux (<0.05 gC/cm^{2}kyr) exhibit a

large range in NPP (10–35 g C/cm^{2}kyr) and EP (0–10 g C/cm^{2}kyr). Schoepfer et al. (2014) found that if preservation effects on organic carbon could be accounted for using variations in bulk sediment accumulation rates, there were significant relationships between a smaller compilation of TOC Holocene burial and NPP and EP estimates; however, that study relied only on bulk organic carbon accumulation rates and, thus, may have been biased by sediment focusing and/or age model errors in the data included. Furthermore, other synthesis work (LaRowe et al., 2020) suggests that organic carbon preservation is complex and depends on many ecological factors in addition to oxygen levels and bulk sedimentation rate.

With regard to Ba_{xs}, we found a weak but significant positive linear correlation with EP and no significant relationship with NPP. Schoepfer et al. (2014) also found no significant relationships between a smaller data compilation of bulk Ba_{xs} accumulation rates and estimates of NPP and EP. Dymond et al. (1992) noted that some preservation effects were apparent in early comparisons between Ba_{xs} in the sediments of different basins and these authors proposed a correction-scheme for Ba preservation effects based on the bulk accumulation rate and the dissolved Ba content in deep waters which varies from basin to basin. Schoepfer et al. (2014) attempted those corrections and still did not find a signficant relationship with productivity patterns. In the present study, we do not have bulk accumulation rates in the data set and thus cannot attempt the Dymond et al. correction; however, we do show that Th-normalized Ba fluxes, which should get as close as possible to the seafloor rain of Ba_{xs}, still do not show a strong relationship with productivity patterns globally. Eagle et al. (2003) did find that relationships between sediment Ba_{xs} and productivity indicators appeared to vary between basins. It is beyond the scope of this study to investigate the possible regional relationships in Ba_{xs} flux but this could be done in future work.

The general conclusion we can draw from this comparison is that productivity indicators such as the flux of opal, TOC and Ba_{xs} are not simply related to the spatial pattern of productivity in the global ocean and likely several preservational effects must modulate their burial fluxes in ways that need further investigation. In the case of opal, there is a known divergence in production patterns, as diatoms, the main producers of biogenic opal, have a distinct biogeography compared to net primary production (e.g., Kostadinov et al., 2010, 2016). Ba_{xs} may have preservation effects that are yet to be fully understood, likely involving the effects of water column undersaturation, bulk mass accumulation rates and the redox state of the sediments. Furthermore, the uncertainties associated with the lithogenic correction on bulk Ba concentrations may obscure relationships with biogenic barite. These results do not preclude, however, the use of these proxies at individual sites or perhaps regional studies in which the change in the proxy with time is interpreted as a change in productivity. The present analysis is focused on global deep-sea spatial patterns as opposed to temporal patterns. Furthermore, average fluxes over the Holocene could considerably differ from satellite-derived productivity estimates which are based mainly on data from the past 20 years. Lastly, the NPP and EP products we have chosen, although state-of-the-art, still contain uncertainty themselves, for example, in matching field measurements (DeVries & Weber, 2017; Silsbe et al., 2016). Thus, there are limits to our ability to evaluate the extent to which biological productivity patterns are embedded within the distribution of the proxy burial rates.

4.3. Imprints of Deep Particulate Flux in Sedimentary Fluxes

While it proved challenging to find the imprint of near surface productivity in our sedimentary database, we explored the relationship of our burial fluxes to subsurface particle fluxes. Deep particle fluxes have undergone some regeneration/dissolution processes since being exported from the surface but have not yet experienced diagenesis at the seafloor while being buried. The knowledge of deep particulate flux is much more limited than either surface or bottom fluxes, but this information is critical especially for the interpretation of paleo-productivity proxies. The information we have is mainly limited to sediment trap studies, although the GEOTRACES program is currently mapping out deep particulate fluxes on transect cruise studies using in-situ pumped particulate ^{230}Th (Hayes et al., 2018; Pavia et al., 2019).

For our comparison here, we use the deep sediment trap compilation of Honjo et al. (2008), that compiled available sediment trap data from 135 sites for $CaCO_3$, opal and TOC and normalized all the data to a common depth of 2 km, or the mesopelagic-bathypelagic boundary (Figure S13). The sedimentary $CaCO_3$ fluxes demonstrated a clear negative relationship (linear correlation $r = 0.53$, $p < 0.01$) with depth, consistent with

the water depth preservation control of $CaCO_3$ solubility. For opal and TOC, we compared the sediment trap fluxes with the geographically closest sedimentary flux that had a water depth of 2–3 km.

Opal preservation was best, in terms of the ratio of burial flux to sediment trap flux, in the Southern Ocean and the equatorial Pacific. In the AESOPS Southern Ocean transect at 170°W, it was found that the ratio of burial to water column particulate opal flux was related to a function of both bulk sedimentation rate and particulate opal flux (Sayles et al., 2001). Some estimate of the bulk sedimentation rates at the sediment flux sites would be needed to assess this model here. The sediment trap opal fluxes were positively correlated with their corresponding opal burial fluxes (burial opal flux = 0.077 ± 0.013* sediment trap opal flux + 0.13 ± 0.03 [g/cm^{2}kyr], $r = 0.51$, $p < 0.01$; Figure S14). The slope of this line implies an overall preservation of 7.7 ± 1.3% of particulate opal rain during burial. This is close to a recent global estimate of preservation of benthic opal rain at the seafloor of 8.0% (Tréguer & De La Rocha, 2013), but our estimate is not precise enough to infer further about the degree of opal dissolution between 2 km and the seafloor.

As with opal, the sedimentary TOC fluxes were correlated, albeit weakly, with the TOC trap fluxes (burial TOC flux = 0.030 ± 0.010 * sediment trap TOC flux + 0.0098 ± 0.0014 [g/cm^{2}kyr], $r = 0.37$, $p < 0.01$; Figure S14). The slope of this line implies an overall preservation of 3 ± 1% of organic carbon rain during burial. This is higher than the often quoted 1% preservation of organic carbon export (e.g., (Hain et al., 2014)) but, of course, our comparison here represents a relatively limited number of sites.

As more water column particulate fluxes become available, particularly from understudied regions, the exercises shown here demonstrate how the sedimentary flux database will be valuable in evaluating preservation controls on key components of the ocean's biogeochemical cycles.

5. Conclusions

In this study, we have prepared an updated global marine sediment composition database, including major and minor components, covering many marginal seas that were previous data gaps. We further demonstrated how a global compilation of Holocene Th-normalized fluxes can be used to estimate the flux of sedimentary components in the deep sea. This allowed us to compute global deep-sea burial rates of $CaCO_3$, opal, TOC, Hg, and Ba_{xs}. Our estimate of deep-seal opal burial is roughly a factor of 2 greater than from previous estimates and suggests roughly equal magnitude in deep-sea and continental margin Si burial. The other burial rates derived here will provide a quantitative target for ocean biogeochemical models. We also investigated preservation effects in the relationship between surface productivity, export productivity, deep particulate flux and sedimentary fluxes. We found that sedimentary Fe fluxes represent a mixture of bulk lithogenic burial flux, coastal enrichment and hydrothermal input. The spatial pattern of some commonly used paleoproxies (TOC, biogenic opal, and Ba_{xs} flux) demonstrated weak relationships with satellite-based productivity estimates. Finally, the understanding of preservation effects on these paleoproxies may significantly improve as more detailed information on deep particulate fluxes can be compared to the sedimentary fluxes compiled here.

Data Availability Statement

The new and compiled data reported here are available at the NOAA Paleoclimatology database (https://www.ncdc.noaa.gov/paleo/study/30512).

Acknowledgments
This study was supported by the Past Global Changes (PAGES) project, which in turn received support from the Swiss Academy of Sciences and the US-NSF. The work grew out of a 2018 workshop in Aix-Marseille, France, funded by PAGES, GEOTRACES, SCOR, US-NSF, Aix Marseille Université, and John Cantle Scientific, and the authors would like to acknowledge all attendees of this meeting. The authors acknowledge the participants of the 68th cruise of RV *Akademik Mstislav Keldysh* for helping acquire samples. Christopher T. Hayes acknowledges support from US-NSF awards 1658445 and 1737023. Some data compilation on Arctic shelf seas was supported by the Russian Science Foundation, grant number 20-17-00157. This work was also supported through project CRESCENDO (grant no. 641816, European Commission). Zanna Chase acknowledges support from the Australian Research Council's *Discovery Projects* funding scheme (project DP180102357). Christopher R. German acknowledges US-NSF awards 1235248 and 1234827. Some colorbars used in the figures were designed by Kristen Thyng et al. (2016) and Patrick Rafter. Two anonymous reviewers are acknowledged for constructive reviews.

References

Amos, H. M., Jacob, D. J., Kocman, D., Horowitz, H. M., Zhang, Y., Dutkiewicz, S., et al. (2014). Global biogeochemical implications of mercury discharges from rivers and sediment burial. *Environmental Science & Technology*, *48*(16), 9514–9522. https://doi.org/10.1021/es502134t

Anderson, R. F. (2020). GEOTRACES: Accelerating research on the marine biogeochemical cycles of trace elements and their isotopes. *Annual Review of Marine Science*, *12*, 9.1–9.37. https://doi.org/10.1146/annurev-marine-010318-095123

Archer, D. E. (1996). An atlas of the distribution of calcium carbonate in sediments of the deep sea. *Global Biogeochemical Cycles*, *10*(1), 159–174. https://doi.org/10.1029/95gb03016

Arrhenius, G., & Bonatti, E. (1965). Neptunism and vulcanism in the ocean. *Progress in Oceanography*, *3*, 7–22. https://doi.org/10.1016/0079-6611(65)90005-4

Bacon, M. P. (1984). Glacial to interglacial changes in carbonate and clay sedimentation in the Atlantic Ocean estimated from ^{230}Th measurements. *Chemical Geology*, *46*, 97–111. https://doi.org/10.1016/0009-2541(84)90183-9

Berelson, W. M., Anderson, R. F., Dymond, J., DeMaster, D., Hammond, D. E., Collier, R., et al. (1997). Biogenic budgets of particle rain, benthic remineralization and sediment accumulation in the equatorial Pacific. *Deep Sea Research Part II: Topical Studies in Oceanography*, *44*(9–10), 2251–2282. https://doi.org/10.1016/s0967-0645(97)00030-1

Berger, W. H. (1974). Deep-Sea Sedimentation. In C. Drake, & C. Burk (Eds.), *The geology of continental margins* (pp. 213–241). Springer-Verlag Berlin Heidelberg. https://doi.org/10.1007/978-3-662-01141-6

Bianchi, T. S., Cui, X., Blair, N. E., Burdige, D. J., Eglinton, T. I., & Galy, V. (2018). Centers of organic carbon burial and oxidation at the land-ocean interface. *Organic Geochemistry*, *115*, 138–155. https://doi.org/10.1016/j.orggeochem.2017.09.008

Bianchi, T. S., Schreiner, K. M., Smith, R. W., Burdige, D. J., Woodard, S., & Conley, D. J. (2016). Redox effects on organic matter storage in coastal sediments during the Holocene: A biomarker/proxy perspective. *Annual Review of Earth and Planetary Sciences*, *44*(1), 295–319. https://doi.org/10.1146/annurev-earth-060614-105417

Bishop, J. K. B. (1988). The barite-opal-organic carbon association in oceanic particulate matter. *Nature*, *332*(6162), 341–343. https://doi.org/10.1038/332341a0

Bisutti, I., Hilke, I., & Raessler, M. (2004). Determination of total organic carbon—An overview of current methods. *TRAC Trends in Analytical Chemistry*, *23*(10–11), 716–726. https://doi.org/10.1016/j.trac.2004.09.003

Bonan, G. B., & Doney, S. C. (2018). Climate, ecosystems, and planetary futures: The challenge to predict life in Earth system models. *Science*, *359*(6375). https://doi.org/10.1126/science.aam8328

Boström, K., Peterson, M. N. A., Joensuu, O., & Fisher, D. E. (1969). Aluminum-poor ferromanganoan sediments on active oceanic ridges. *Journal of Geophysical Research*, *74*(12), 3261–3270. https://doi.org/10.1029/jb074i012p03261

Bowman, K. L., Hammerschmidt, C. R., Lamborg, C. H., & Swarr, G. (2015). Mercury in the North Atlantic Ocean: The U.S. GEOTRACES zonal and meridional sections. *Deep Sea Research Part II: Topical Studies in Oceanography*, *116*, 251–261. https://doi.org/10.1016/j.dsr2.2014.07.004

Bowman, K. L., Hammerschmidt, C. R., Lamborg, C. H., Swarr, G. J., & Agather, A. M. (2016). Distribution of mercury species across a zonal section of the eastern tropical South Pacific Ocean (U.S. GEOTRACES GP16). *Marine Chemistry*, *186*, 156–166. https://doi.org/10.1016/j.marchem.2016.09.005

Broecker, W. S., & Peng, T.-H. (1982). *Tracers in the Sea*. Palisades, NY: Eldigio Press. Retrieved from https://www.ldeo.columbia.edu/~broecker/Home_files/TracersInTheSea_searchable.pdf

Budko, D. F., Demina, L. L., Novichkova, E. A., Polyakova, Y. I., & Kravchishina, M. D. (2019). Postglacial sedimentation in the White Sea (Northwestern Russia) reconstructed by integrated microfossil and geochemical data. *Quaternary Research*, 1–14. https://doi.org/10.1017/qua.2019.49

Burdige, D. J. (2005). Burial of terrestrial organic matter in marine sediments: A re-assessment. *Global Biogeochemical Cycles*, *19*(4), 1–7. https://doi.org/10.1029/2004gb002368

Burdige, D. J. (2007). Preservation of organic matter in marine sediments: Controls, mechanisms, and an imbalance in sediment organic carbon budgets? *Chemical Reviews*, *107*(2), 467–485. https://doi.org/10.1021/cr050347q

Cartapanis, O., Bianchi, D., Jaccard, S. L., & Galbraith, E. D. (2016). Global pulses of organic carbon burial in deep-sea sediments during glacial maxima. *Nature Communications*, *7*. https://doi.org/10.1038/ncomms10796

Cartapanis, O., Galbraith, E. D., Bianchi, D., & Jaccard, S. L. (2018). Carbon burial in deep-sea sediment and implications for oceanic inventories of carbon and alkalinity over the last glacial cycle. *Climate of the Past*, *14*(11), 1819–1850. https://doi.org/10.5194/cp-14-1819-2018

Catubig, N. R., Archer, D. E., Francois, R., DeMenocal, P., Howard, W., & Yu, E.-F. (1998). Global deep-sea burial rate of calcium carbonate during the last glacial maximum. *Paleoceanography*, *13*(3), 298–310. https://doi.org/10.1029/98pa00609

Chase, Z., Anderson, R. F., Fleisher, M. Q., & Kubik, P. W. (2002). The influence of particle composition and particle flux on scavenging of Th, Pa and Be in the ocean. *Earth and Planetary Science Letters*, *204*, 215–229. https://doi.org/10.1016/s0012-821x(02)00984-6

Chase, Z., Kohfeld, K. E., & Matsumoto, K. (2015). Controls on biogenic silica burial in the Southern Ocean. *Global Biogeochemical Cycles*, *29*, 1599–1616. https://doi.org/10.1002/2015gb005186

Conley, D. J. (1998). An interlaboratory comparison for the measurement of biogenic silica in sediments. *Marine Chemistry*, *63*(1–2), 39–48. https://doi.org/10.1016/s0304-4203(98)00049-8

Cossa, D., Averty, B., & Pirrone, N. (2009). The origin of methylmercury in open mediterranean waters. *Limnology & Oceanography*, *54*(3), 837–844. https://doi.org/10.4319/lo.2009.54.3.0837

Cossa, D., Heimbürger, L.-E., Pérez, F. F., García-Ibáñez, M. I., Sonke, J. E., Planquette, H., et al. (2018). Mercury distribution and transport in the North Atlantic Ocean along the GEOTRACES-GA01 transect. *Biogeosciences*, *15*(8), 2309–2323. https://doi.org/10.5194/bg-15-2309-2018

Costa, K. M., Hayes, C. T., Anderson, R. F., Pavia, F. J., Bausch, A., Deng, F., et al. (2020). ^{230}Th normalization: New insights on an essential tool for quantifying sedimentary fluxes in the modern and Quaternary ocean. *Paleoceanography and Paleoclimatology*, *35*(2), e2019PA003820. https://doi.org/10.1029/2019pa003820

Dehairs, F., Chesselet, R., & Jedwab, J. (1980). Discrete suspended particles of barite and the barium cycle in the open ocean. *Earth and Planetary Science Letters*, *49*, 528–550. https://doi.org/10.1016/0012-821x(80)90094-1

DeMaster, D. J. (1981). The supply and accumulation of silica in the marine environment. *Geochimica et Cosmochimica Acta*, *45*, 1715–1732. https://doi.org/10.1016/0016-7037(81)90006-5

DeMaster, D. J. (2002). The accumulation and cycling of biogenic silica in the Southern Ocean: Revisiting the marine silica budget. *Deep Sea Research Part II: Topical Studies in Oceanography*, *49*, 3155–3167. https://doi.org/10.1016/s0967-0645(02)00076-0

DeMaster, D. J. (2019). The global marine silica budget: Sources and sinks. *Encyclopedia of Ocean Sciences* (3rd ed., pp. 473–483). Elsevier. https://doi.org/10.1016/b978-0-12-409548-9.10799-7

Demina, L. L., Novichkova, E. A., Lisitzin, A. P., & Kozina, N. V. (2019). Geochemical signatures of paleoclimate changes in the sediment cores from the Gloria and Snorri drifts (Northwest Atlantic) over the Holocene-Mid Pleistocene. *Geosciences*, *9*(432), 1–19. https://doi.org/10.3390/geosciences9100432

DeVries, T., & Weber, T. (2017). The export and fate of organic matter in the ocean: New constraints from combining satellite and oceanographic tracer observations. *Global Biogeochemical Cycles*, *31*(3), 535–555. https://doi.org/10.1002/2016gb005551

Dickens, G. R., Fewless, T., Thomas, E., & Bralower, T. J. (2003). Excess barite accumulation during the Paleocene-Eocene Thermal Maximum: Massive input of dissolved barium from seafloor gas hydrate reservoirs. In S. L. Wing, P. D. Gingerich, B. Schmitz, & E. Thomas (Eds.), *Causes and Consequences of Globally Warm Climates in the Early Paleogene*, (Vol. 369, pp. 11–23). Geological Society of America. https://doi.org/10.1130/0-8137-2369-8.11

Dunne, J. P., Hales, B., & Toggweiler, J. R. (2012). Global calcite cycling constrained by sediment preservation controls. *Global Biogeochemical Cycles*, *26*(3), 1–14. https://doi.org/10.1029/2010gb003935

Dunne, J. P., Sarmiento, J. L., & Gnanadesikan, A. (2007). A synthesis of global particle export from the surface ocean and cycling through the ocean interior and on the seafloor. *Global Biogeochemical Cycles*, *21*, 1–16. https://doi.org/10.1029/2006gb002907

Dymond, J., & Collier, R. (1996). Particulate barium fluxes and their relationships to biological productivity. *Deep Sea Research Part II: Topical Studies in Oceanography*, *43*(4–6), 1283–1308. https://doi.org/10.1016/0967-0645(96)00011-2

Dymond, J., Suess, E., & Lyle, M. (1992). Barium in deep-sea sediment: A geochemical proxy for paleoproductivity. *Paleoceanography*, *7*(2), 163–181. https://doi.org/10.1029/92pa00181

Eagle, M., Paytan, A., Arrigo, K. R., van Dijken, G., & Murray, R. W. (2003). A comparison between excess barium and barite as indicators of carbon export. *Paleoceanography*, *18*(1). https://doi.org/10.1029/2003pa000922

Edmond, J. M., Boyle, E. D., Drummond, D., Grant, B., & Mislick, T. (1978). Desorption of barium in the plume of the Zaire (Congo) river. *Netherlands Journal of Sea Research*, *12*(3–4), 324–328. https://doi.org/10.1016/0077-7579(78)90034-0

Fitzsimmons, J. N., John, S. G., Marsay, C. M., Hoffman, C. L., Nicholas, S. L., Toner, B. M., et al. (2017). Iron persistence in a distal hydrothermal plume supported by dissolved-particulate exchange. *Nature Geoscience*, *10*, 195–201. https://doi.org/10.1038/ngeo2900

Flanders Marine Institute, (2009). *Longhurst provinces*. https://www.marineregions.org/sources.php#longhurst

François, R., Frank, M., Rutgers van der Loeff, M. M., & Bacon, M. P. (2004). Th normalization: An essential tool for interpreting sedimentary fluxes during the late Quaternary. *Paleoceanography*, *19*, 1–16. https://doi.org/10.1029/2003pa000939

François, R., Honjo, S., Manganini, S. J., & Ravizza, G. E. (1995). Biogenic barium fluxes to the deep sea: Implications for paleoproductivity reconstruction. *Global Biogeochemical Cycles*, *9*(2), 289–303. https://doi.org/10.1029/95gb00021

German, C. (2017). *Core-top (0-1cm) sediment data collected by monocore from R/V Thomas G. Thompson TN303 (GP16; EPZT) GEOTRACES cruise from November to December 2013 (GEOTRACES EPZT project). Biological and chemical oceanography data management office (BCO-DMO), 2017-04–06*. Retrieved from http://lod.bco-dmo.org/id/dataset/686982

Griffith, E. M., & Paytan, A. (2012). Barite in the ocean—Occurrence, geochemistry and palaeoceanographic applications. *Sedimentology*, *59*(6), 1817–1835. https://doi.org/10.1111/j.1365-3091.2012.01327.x

Hain, M. P., Sigman, D. M., & Haug, G. H. (2014). *The biological pump in the past: The oceans and marine geochemistry* (2nd ed., Vol. 8). Elsevier Ltd. https://doi.org/10.1016/B978-0-08-095975-7.00614-8

Hayes, C. T., Anderson, R. F., Fleisher, M. Q., Serno, S., Winckler, G., & Gersonde, R. (2014). Biogeography in ^{231}Pa/^{230}Th ratios and a balanced ^{231}Pa budget for the Pacific Ocean. *Earth and Planetary Science Letters*, *391*, 307–318. https://doi.org/10.1016/j.epsl.2014.02.001

Hayes, C. T., Anderson, R. F., Fleisher, M. Q., Vivancos, S. M., Lam, P. J., Ohnemus, D. C., et al. (2015). Intensity of Th and Pa scavenging partitioned by particle chemistry in the North Atlantic Ocean. *Marine Chemistry*, *170*, 49–60. https://doi.org/10.1016/j.marchem.2015.01.006

Hayes, C. T., Black, E. E., Anderson, R. F., Baskaran, M., Buesseler, K. O., Charette, M. A., et al. (2018). Flux of particulate elements in the North Atlantic Ocean constrained by multiple radionuclides. *Global Biogeochemical Cycles*, *32*(12), 1738–1758. https://doi.org/10.1029/2018gb005994

Hayes, C. T., McGee, D., Mukhopadhyay, S., Boyle, E. A., & Maloof, A. C. (2017). Helium and thorium isotope constraints on African dust transport to the Bahamas over recent millennia. *Earth and Planetary Science Letters*, *457*. https://doi.org/10.1016/j.epsl.2016.10.031

Honjo, S., Dymond, J., Collier, R., & Manganini, S. J. (1995). Export production of particles to the interior of the equatorial Pacific Ocean during the 1992 EqPac experiment. *Deep Sea Research Part II: Topical Studies in Oceanography*, *42*(2), 831–870. https://doi.org/10.1016/0967-0645(95)00034-n

Honjo, S., Manganini, S. J., Krishfield, R. A., & Francois, R. (2008). Particulate organic carbon fluxes to the ocean interior and factors controlling the biological pump: A synthesis of global sediment trap programs since 1983. *Progress in Oceanography*, *76*(3), 217–285. https://doi.org/10.1016/j.pocean.2007.11.003

Horner, T., Little, S., Conway, T., Farmer, J., Hertzberg, J., Lough, A., et al. (2020). Bioactive trace metals and their isotopes as paleoproductivity proxies: An assessment using GEOTRACES-era data. *Earth and Space Science Open Archive*. https://doi.org/10.1002/essoar.10504252.1

Ingamells, C. O. (1970). Lithium metaborate flux in silicate analysis. *Analytica Chimica Acta*, *52*, 323–334. https://doi.org/10.1016/s0003-2670(01)80963-6

Jahnke, R. A. (1996). The global ocean flux of particulate organic carbon: Areal distribution and magnitude. *Global Biogeochemical Cycles*, *10*(1), 71–88. https://doi.org/10.1029/95gb03525

Key, R. M., Kozyr, A., Sabine, C. L., Lee, K., Wanninkhof, R., Bullister, J. L., et al. (2004). A global ocean carbon climatology: Results from Global Data Analysis Project (GLODAP). *Global Biogeochemical Cycles*, *18*(4), 1–23. https://doi.org/10.1029/2004gb002247

Kienast, S. S., Winckler, G., Lippold, J., Albani, S., & Mahowald, N. M. (2016). Tracing dust input to the global ocean using thorium isotopes in marine sediments: ThoroMap. *Global Biogeochemical Cycles*, *30*(10), 1526–1541. https://doi.org/10.1002/2016gb005408

Kim, H., Soerensen, A. L., Hur, J., Heimbürger, L.-E., Hahm, D., Rhee, T. S., et al. (2017). Methylmercury mass budgets and distribution characteristics in the Western Pacific Ocean. *Environmental Science & Technology*, *51*(3), 1186–1194. https://doi.org/10.1021/acs.est.6b04238

Klump, J., Hebbeln, D., & Wefer, G. (2000). The impact of sediment provenance on barium-based productivity estimates. *Marine Geology*, *169*(3–4), 259–271. https://doi.org/10.1016/s0025-3227(00)00092-x

Kostadinov, T. S., Milutinović, S., Marinov, I., & Cabré, A. (2016). Carbon-based phytoplankton size classes retrieved via ocean color estimates of the particle size distribution. *Ocean Science*, *12*(3), 561–575. https://doi.org/10.5194/os-12-561-2016

Kostadinov, T. S., Siegel, D. A., & Maritorena, S. (2010). Global variability of phytoplankton functional types from space: Assessment via the particle size distribution. *Biogeosciences*, *7*(10), 3239–3257. https://doi.org/10.5194/bg-7-3239-2010

Kravchishina, M. D., Novigatskii, A. N., Savvichev, A. S., Pautova, L. A., & Lisitsyn, A. P. (2019). Studies on sedimentary systems in the Barents Sea and Norwegian-Greenland basin during Cruise 68 of the R/V Akademik Mstislav Keldysh. *Oceanology*, *59*(1), 158–160. https://doi.org/10.1134/s0001437019010053

Lam, P. J., Doney, S. C., & Bishop, J. K. B. (2011). The dynamic ocean biological pump: Insights from a global compilation of particulate organic carbon, $CaCO_3$, and opal concentration profiles from the mesopelagic. *Global Biogeochemical Cycles*, *25*(3), 1–14. https://doi.org/10.1029/2010gb003868

LaRowe, D. E., Arndt, S., Bradley, J. A., Estes, E. R., Hoarfrost, A., Lang, S. Q., et al. (2020). The fate of organic carbon in marine sediments - New insights from recent data and analysis. *Earth-Science Reviews*, *204*, 103146. https://doi.org/10.1016/j.earscirev.2020.103146

Lee, T. R., Wood, W. T., & Phrampus, B. J. (2019). A machine learning (kNN) approach to predicting global seafloor total organic carbon. *Global Biogeochemical Cycles*, *33*(1), 37–46. https://doi.org/10.1029/2018gb005992

Lisitzin, A. P. (1996). In *Oceanic sedimentation: Lithology and geochemistry*. Washington, DC: American Geophysical Union. https://doi.org/10.1002/9781118665008

Longhurst, A. (1995). Seasonal cycles of pelagic production and consumption. *Progress in Oceanography*, *36*(2), 77–167. https://doi.org/10.1016/0079-6611(95)00015-1

Longhurst, A. R. (2006). *Ecological Geography of the Sea* (2nd ed.). San Diego: Academic Press. ISBN: 9780124555211

Longhurst, A., Sathyendranath, S., Platt, T., & Caverhill, C. (1995). An estimate of global primary production in the ocean from satellite radiometer data. *Journal of Plankton Research*, *17*(6), 1245–1271. https://doi.org/10.1093/plankt/17.6.1245

Maldonado, M., López-Acosta, M., Sitjà, C., García-Puig, M., Galobart, C., Ercilla, G., et al. (2019). Sponge skeletons as an important sink of silicon in the global oceans. *Nature Geoscience*, *12*(10), 815–822. https://doi.org/10.1038/s41561-019-0430-7

Martinez-Ruiz, F., Paytan, A., Gonzalez-Muñoz, M. T., Jroundi, F., Abad, M. M., Lam, P. J., et al. (2019). Barite formation in the ocean: Origin of amorphous and crystalline precipitates. *Chemical Geology*, *511*, 441–451. https://doi.org/10.1016/j.chemgeo.2018.09.011

McGee, D., & Mukhopadhyay, S. (2013). Extraterrestrial He in Sediments: From Recorder of Asteroid Collisions to Timekeeper of Global Environmental Changes. In P. Burnard (Ed.), *The Noble Gases as Geochemical Tracers* (pp. 155–176). Berlin, Heidelberg: Springer. https://doi.org/10.1007/978-3-642-28836-4

McManus, J., Berelson, W. M., Klinkhammer, G. P., Johnson, K. S., Coale, K. H., Anderson, R. F., et al. (1998). Geochemistry of barium in marine sediments: Implications for its use as a paleoproxy. *Geochimica et Cosmochimica Acta*, *62*(21), 3453–3473. https://doi.org/10.1016/s0016-7037(98)00248-8

Mekik, F., & Anderson, R. (2018). Is the core top modern? Observations from the eastern equatorial Pacific. *Quaternary Science Reviews*, *186*, 156–168. https://doi.org/10.1016/j.quascirev.2018.01.020

Milliman, J. D. (1993). Production and accumulation of calcium carbonate in the ocean: Budget of a nonsteady state. *Global Biogeochemical Cycles*, *7*(4), 927–957. https://doi.org/10.1029/93gb02524

Monnin, C., & Cividini, D. (2006). The saturation state of the world's ocean with respect to (Ba,Sr)SO_4 solid solutions. *Geochimica et Cosmochimica Acta*, *70*(13), 3290–3298. https://doi.org/10.1016/j.gca.2006.04.002

Mörth, C.-M., & Backman, J. (2011). Practical steps for improved estimates of calcium carbonate concentrations in deep sea sediments using coulometry. *Limnology and Oceanography: Methods*, *9*, 565–570. https://doi.org/10.4319/lom.2011.9.565

Mortlock, R. A., & Froelich, P. N. (1989). A simple method for the rapid determination of biogenic opal in pelagic marine sediments. *Deep-Sea Research Part A. Oceanographic Research Papers*, *36*(9A), 1415–1426. https://doi.org/10.1016/0198-0149(89)90092-7

Outridge, P. M., Mason, R. P., Wang, F., Guerrero, S., & Heimbürger-Boavida, L. E. (2018). Updated global and oceanic mercury budgets for the United Nations Global Mercury Assessment 2018. *Environmental Science and Technology*, *52*(20), 11466–11477. https://doi.org/10.1021/acs.est.8b01246

Pavia, F. J., Anderson, R. F., Lam, P. J., Cael, B. B., Vivancos, S. M., Fleisher, M. Q., et al. (2019). Shallow particulate organic carbon regeneration in the South Pacific Ocean. *Proceedings of the National Academy of Sciences of the United States of America*, *116*(20), 9753–9758. https://doi.org/10.1073/pnas.1901863116

Pavia, F. J., Anderson, R. F., Vivancos, S., Fleisher, M., Lam, P., Lu, Y., et al. (2018). Intense hydrothermal scavenging of ^{230}Th and ^{231}Pa in the deep Southeast Pacific. *Marine Chemistry*, *201*, 212–228. https://doi.org/10.1016/j.marchem.2017.08.003

Paytan, A., & Griffith, E. M. (2007). Marine barite: Recorder of variations in ocean export productivity. *Deep Sea Research Part II: Topical Studies in Oceanography*, *54*, 687–705. https://doi.org/10.1016/j.dsr2.2007.01.007

Paytan, A., & Kastner, M. (1996). Benthic Ba fluxes in the central Equatorial Pacific, implications for the oceanic Ba cycle. *Earth and Planetary Science Letters*, *142*, 439–450. https://doi.org/10.1016/0012-821x(96)00120-3

Ragueneau, O., Tréguer, P., Leynaert, A., Anderson, R. F., Brzezinski, M. A., Demaster, D. J., et al. (2000). A review of the Si cycle in the modern ocean: recent progress and missing gaps in the application of biogenic opal as a paleoproductivity proxy. *Global and Planetary Change*, *26*, 317–365. https://doi.org/10.1016/s0921-8181(00)00052-7

Rahman, S., Aller, R. C., & Cochran, J. K. (2017). The missing silica sink: Revisiting the marine sedimentary Si cycle using cosmogenic 32 Si. *Global Biogeochemical Cycles*, *31*, 1559–1578. https://doi.org/10.1002/2017gb005746

Reitz, A., Pfeifer, K., De Lange, G. J., & Klump, J. (2004). Biogenic barium and the detrital Ba/Al ratio: A comparison of their direct and indirect determination. *Marine Geology*, *204*(3–4), 289–300. https://doi.org/10.1016/s0025-3227(04)00004-0

Resing, J. A., Sedwick, P. N., German, C. R., Jenkins, W. J., Moffett, J. W., Sohst, B. M., et al. (2015). Basin-scale transport of hydrothermal dissolved metals across the South Pacific Ocean. *Nature*, *523*, 200–203. https://doi.org/10.1038/nature14577

Restreppo, G. A., Wood, W. T., & Phrampus, B. J. (2020). Oceanic sediment accumulation rates predicted via machine learning algorithm: towards sediment characterization on a global scale. *Geo-Marine Letters*, *40*(5), 755–763. https://doi.org/10.1007/s00367-020-00669-1

Reygondeau, G., Longhurst, A., Martinez, E., Beaugrand, G., Antoine, D., & Maury, O. (2013). Dynamic biogeochemical provinces in the Global Ocean. *Global Biogeochemical Cycles*, *27*(4), 1046–1058. https://doi.org/10.1002/gbc.20089

Riedinger, N., Kasten, S., Gröger, J., Franke, C., & Pfeifer, K. (2006). Active and buried authigenic barite fronts in sediments from the Eastern Cape Basin. *Earth and Planetary Science Letters*, *241*(3–4), 876–887. https://doi.org/10.1016/j.epsl.2005.10.032

Rosati, G., Heimbürger, L. E., Melaku Canu, D., Lagane, C., Laffont, L., Rijkenberg, M. J. A., et al. (2018). Mercury in the Black Sea: New insights from measurements and numerical modeling. *Global Biogeochemical Cycles*, *32*(4), 529–550. https://doi.org/10.1002/2017gb005700

Rudnick, R. L., & Gao, S. (2014). Composition of the continental crust. In H. D. Holland, & K. K. Turekian (Eds.), *Treatise on Geochemistry*, (2nd ed, Vol. 4, pp. 1–51). Oxford, UK: Elsevier. https://doi.org/10.1016/B978-0-08-095975-7.00301-6

Sandroni, V., Smith, C. M. M., & Donovan, A. (2003). Microwave digestion of sediment, soils and urban particulate matter for trace metal analysis. *Talanta*, *60*(4), 715–723. https://doi.org/10.1016/s0039-9140(03)00131-0

Sayles, F. L., Martin, W. R., Chase, Z., & Anderson, R. F. (2001). Benthic remineralization and burial of biogenic SiO_2, $CaCO_3$, organic carbon, and detrital material in the Southern Ocean along a transect at 170° West. *Deep Sea Research Part II: Topical Studies in Oceanography*, *48*, 4323–4383. https://doi.org/10.1016/s0967-0645(01)00091-1

Schoepfer, S. D., Shen, J., Wei, H., Tyson, R. V., Ingall, E., & Algeo, T. J. (2014). Total organic carbon, organic phosphorus, and biogenic barium fluxes as proxies for paleomarine productivity. *Earth-Science Reviews*. *149*, 23–52. https://doi.org/10.1016/j.earscirev.2014.08.017

Seiter, K., Hensen, C., Schroter, J., & Zabel, M. (2004). Organic carbon content in surface sediments — defining regional provinces. *Deep-Sea Research I*, *51*. 2001–2026. https://doi.org/10.1016/j.dsr.2004.06.014

Serno, S., Winckler, G., Anderson, R. F., Hayes, C. T., Ren, H., Gersonde, R., et al. (2014). Using the natural spatial pattern of marine productivity in the Subarctic North Pacific to evaluate paleoproductivity proxies. *Paleoceanography*, *29*, 438–453. https://doi.org/10.1002/2013pa002594

Silsbe, G. M., Behrenfeld, M. J., Halsey, K. H., Milligan, A. J., & Westberry, T. K. (2016). The CAFE model: A net production model for global ocean phytoplankton. *Global Biogeochemical Cycles*, *30*, 1756–1777. https://doi.org/10.1002/2016gb005521

Sternberg, E., Tang, D., Ho, T.-Y., Jeandel, C., & Morel, F. M. M. (2005). Barium uptake and adsorption in diatoms. *Geochimica et Cosmochimica Acta*, *69*(11), 2745–2752. https://doi.org/10.1016/j.gca.2004.11.026

Suman, D. O., & Bacon, M. P. (1989). Variations in Holocene sedimentation in the North American Basin determined from ^{230}Th measurements. *Deep-Sea Research Part A. Oceanographic Research Papers*, *36*(6), 869–878. https://doi.org/10.1016/0198-0149(89)90033-2

Tesán Onrubia, J. A., Petrova, M. V., Puigcorbé, V., Black, E. E., Valk, O., Dufour, A., et al. (2020). Mercury Export Flux in the Arctic Ocean Estimated from ^{234}Th/^{238}U Disequilibria. *ACS Earth and Space Chemistry*, *4*(5), 795–801. https://doi.org/10.1021/acsearthspacechem.0c00055

Thyng, K., Greene, C., Hetland, R., Zimmerle, H., & DiMarco, S. (2016). True colors of oceanography: Guidelines for effective and accurate colormap selection. *Oceanography*, *29*(3), 9–13. https://doi.org/10.5670/oceanog.2016.66

Torres, M. E., Brumsack, H. J., Bohrmann, G., & Emeis, K. C. (1996). Barite fronts in continental margin sediments: A new look at barium remobilization in the zone of sulphate reduction and formation of heavy barites in diagenetic fronts. *Chemical Geology*, *127*(1–3), 125–139. https://doi.org/10.1016/0009-2541(95)00090-9

Tréguer, P. J., & De La Rocha, C. L. (2013). The world ocean silica cycle. *Annual Review of Marine Science*, *5*, 477–501. https://doi.org/10.1146/annurev-marine-121211-172346

Tréguer, P. J., Nelson, D. M., Van Bennekom, A. J., DeMaster, D. J., Leynaert, A., & Queguiner, B. (1995). The silica balance in the world ocean: A reestimate. *Science*, *268*, 375–379. https://doi.org/10.1126/science.268.5209.375

Tréguer, P. J., Sutton, J. N., Brzezinski, M., Charette, M. A., DeVries, T., Dutkiewicz, S., et al. (2021). Reviews and syntheses: The biogeochemical cycle of silicon in the modern ocean. *Biogeosciences*, *18*, 1269–1289. https://doi.org/10.5194/bg-18-1269-2021

Van Beek, P., Reyss, J.-L., Bonte, P., & Schmidt, S. (2003). Sr/Ba in barite: A proxy of barite preservation in marine sediments? *Marine Geology*, *199*(3–4), 205–220. https://doi.org/10.1016/s0025-3227(03)00220-2

Von Damm, K. L., Edmond, J. M., Grant, B., Measures, C. I., Walden, B., & Weiss, R. F. (1985). Chemistry of submarine hydrothermal solutions at 21°N, East Pacific Rise. *Geochimica et Cosmochimica Acta*, *49*(11), 2197–2220. https://doi.org/10.1016/0016-7037(85)90222-4

White, W. M., & Klein, E. M. (2013). Composition of the oceanic crust. In *Treatise on geochemistry*, (2nd ed., Vol. 4, pp. 457–496). Elsevier Ltd. https://doi.org/10.1016/B978-0-08-095975-7.00315-6

Wien, K., Wissmann, D., Kölling, M., & Schulz, H. D. (2005). Fast application of X-ray fluorescence spectrometry aboard ship: How good is the new portable Spectro Xepos analyser? *Geo-Marine Letters*, *25*(4), 248–264. https://doi.org/10.1007/s00367-004-0206-x

Yuan, C.-g., Shi, J.-b., He, B., Liu, J.-f., Liang, L.-n., & Jiang, G.-b. (2004). Speciation of heavy metals in marine sediments from the East China Sea by ICP-MS with sequential extraction. *Environment International*, *30*(6), 769–783. https://doi.org/10.1016/j.envint.2004.01.001

Yu, J., Anderson, R. F., Jin, Z., Menviel, L., Zhang, F., Ryerson, F. J., et al. (2014). Deep South Atlantic carbonate chemistry and increased interocean deep water exchange during last deglaciation. *Quaternary Science Reviews*, *90*, 80–89. https://doi.org/10.1016/j.quascirev.2014.02.018

Yu, J., Broecker, W. S., Elderfield, H., Jin, Z., McManus, J., & Zhang, F. (2010). Loss of carbon from the deep sea since the last glacial maximum. *Science*, *330*, 1084–1087. https://doi.org/10.1126/science.1193221

Zhang, Y., Jacob, D. J., Dutkiewicz, S., Amos, H. M., Long, M. S., & Sunderland, E. M. (2015). Biogeochemical drivers of the fate of riverine mercury discharged to the global and Arctic oceans. *Global Biogeochemical Cycles*, *29*, 854–864. https://doi.org/10.1002/2015gb005124